



OpenAIR@RGU

The Open Access Institutional Repository at Robert Gordon University

<http://openair.rgu.ac.uk>

This is an author produced version of a paper published in

Journal of Thermal Spray Technology (ISSN 1059-9630, eISSN 1544-1016)

This version may not include final proof corrections and does not include published layout or pagination.

Citation Details

Citation for the version of the work held in 'OpenAIR@RGU':

AHMED, R., FAISAL, N. H, AL-ANAZI, N. M., AL-MUTAIRI, S., TOMA, F.-L., BERGER, L.-M., POTTHOFF, A., ELAKWAH, Y. O. and GOOSEN, M. F. A., 2015. Structure property relationship of suspension thermally sprayed WC-Co nanocomposite coatings. Available from *OpenAIR@RGU*. [online]. Available from: <http://openair.rgu.ac.uk>

Citation for the publisher's version:

AHMED, R., FAISAL, N. H, AL-ANAZI, N. M., AL-MUTAIRI, S., TOMA, F.-L., BERGER, L.-M., POTTHOFF, A., ELAKWAH, Y. O. and GOOSEN, M. F. A., 2015. Structure property relationship of suspension thermally sprayed WC-Co nanocomposite coatings. *Journal of Thermal Spray Technology*, 24 (3), pp. 357-377.

Copyright

Items in 'OpenAIR@RGU', Robert Gordon University Open Access Institutional Repository, are protected by copyright and intellectual property law. If you believe that any material held in 'OpenAIR@RGU' infringes copyright, please contact openair-help@rgu.ac.uk with details. The item will be removed from the repository while the claim is investigated.

“The final publication is available at Springer via <http://dx.doi.org/10.1007/s11666-014-0174-2>”.

Please note that the illustrative material which accompanied this text is provided in a separate file.

Structure Property Relationship of Suspension Thermally Sprayed WC-Co Nanocomposite Coatings

R. Ahmed ^{a,b1}, N. H. Faisal ^{a,c}, Nayef M. Al-Anazi ^d, S. Al-Mutairi ^d, F.-L. Toma ^e, L.-M. Berger ^f, A. Potthoff ^f, E. K. Polychroniadis ^g, M. Sall ^g, D. Chaliampalias ^g, M. F. A. Goosen ^h

^a College of Engineering, Alfaisal University, P.O. Box 50927, Riyadh, 11533, Saudi Arabia

^b School of Engineering and Physical Sciences, Heriot-Watt University, Edinburgh, EH14 4AS, UK

^c School of Engineering, Robert Gordon University, Garthdee Road, Aberdeen, AB10 7GJ, UK

^d Materials Performance Unit, Research & Development Centre, Saudi Aramco, Dhahran, 31311, Saudi Arabia

^e Fraunhofer Institute for Material and Beam Technology - IWS, Winterbergstrasse 28, D-01277 Dresden, Germany

^f Fraunhofer Institute for Ceramic Technologies and Systems - IKTS, Winterbergstrasse 28, D-01277 Dresden, Germany

^g Department of Physics, Aristotle University of Thessaloniki, Thessaloniki 54124, Greece

^h Office of Research & Graduate Studies, Alfaisal University, P.O. Box 50927, Riyadh 11533, Saudi Arabia

ABSTRACT

Tribomechanical properties of nanostructured coatings deposited by Suspension High Velocity Oxy-Fuel (S-HVOF) and conventional HVOF (Jet Kote) spraying were evaluated. Nanostructured S-HVOF coatings were obtained via ball milling of the agglomerated and sintered WC-12Co feedstock powder, which were deposited via an aqueous based suspension using modified HVOF (TopGun) process. Microstructural evaluations of these hardmetal coatings included Transmission Electron Microscopy (TEM), X-ray Diffraction (XRD) and Scanning Electron Microscopy (SEM) equipped with Energy Dispersive X-ray Spectroscopy (EDX). The nanohardness and modulus of the coated specimens was investigated using a diamond Berkovich nanoindenter. Sliding wear tests were conducted using a ball-on-flat test rig. Results indicated that low porosity coatings with nanostructured features were obtained. High carbon loss was observed, but coatings showed a high hardness up to 1000 HV0.3. S-HVOF coatings also showed improved sliding wear and friction behavior, which was attributed to nanosized particles reducing ball wear in three body abrasion, and support of metal matrix due to uniform distribution of nanoparticles in the coating microstructure.

Keywords: Nanostructured coating, WC-Co coating, Suspension spraying, nanoindentation, wear, tribology.

¹ Corresponding author (R.Ahmed@hw.ac.uk;

1. INTRODUCTION

Overlay hardmetal and ceramic thermal spray coatings are frequently employed in wear and corrosion resistance applications [1-10]. Coatings deposited by techniques such as high velocity oxy-fuel (HVOF), air plasma (APS), detonation gun (D-Gun), and wire-arc spraying are used in many industrial applications ranging from aerospace, transportation, off-shore and civil engineering to biomedical industries. These applications rely on the high abrasion, sliding, corrosion, and erosion wear resistance of hardmetal and oxide (e.g. Cr_2O_3 , $\text{Al}_2\text{O}_3\text{-TiO}_2$) coatings [5-9]. Hardmetals, such as commercially available tungsten carbide-cobalt (WC-Co) compositions, combine the properties of hard particles with those of a ductile binder matrix. The wear resistance of these composites depends on the interaction of the two surfaces in relative motion and the stress profile of the application. Other combinations such as WC-Co-Cr, $\text{Cr}_3\text{C}_2\text{-NiCr}$ WC-NiCrBSi, WC-NiMoCrFeCo are also commercially available [5-9, 11-16]. Tungsten carbide (WC) is a unique chemical compound, for instance, it is approximately three times stiffer than steel. Tribomechanical properties such as hardness, wear resistance, and strength are influenced primarily by the size and distribution of WC grains, the volume fraction and thermo-mechanical properties of the metal matrix, and post-treatments of the composite hardmetal coating [11-19]. As noted by Fang *et al.* [4] the cutting tool industry has already seen the benefits of fine grain WC-Co hardmetals. Improvements over the existing performance are therefore inevitable from nanocomposite materials.

Recent advances in thermal spray technology utilize nanocomposite materials for both hardmetals such as $\text{Cr}_3\text{C}_2\text{-NiCr}$, WC-Co [13, 19-21], and ceramics such as alumina-yttria-stabilised zirconia (YSZ) and hydroxyapatite [22-23], which offer the potential of higher mechanical strength and improved thermal and wear resistance properties in comparison to conventional materials. Past two decades have seen extensive research in optimizing the coating powder characteristics, process parameters, and post-treatments of hardmetal coatings [9, 11-16]. Most research however has related to coatings prepared from agglomerated and sintered powders, with the average particle size ranging from 10 μm to 50 μm . The properties of hardmetal coatings based on WC and Cr_3C_2 depend on the prevention and minimization of carbon loss, which in particular is critical for

nanosized composites. Optimization of these coatings have resulted in coating microstructure with negligible porosity, high fracture toughness and minimization of secondary carbide phases [1-9, 11-16]. In these previous investigations, the problems associated with the injection of submicron particles have been addressed via agglomeration of nanoparticles to micron sized powder for thermal spraying [1, 3, 11-13, 15, 20-21, 24-30].

Thermal spraying with suspensions is a process where water [1, 10, 24-25], ethanol [1, 23], or mixtures such as ethanol and ethylene glycol [2] have been employed to introduce nanosized particles directly into the thermal spray process. Oxides including Al_2O_3 and TiO_2 [10], alumina-YSZ [23], YSZ [1, 24] and coatings for solid oxide fuel cells [1] have been successfully deposited with liquid suspension spraying. Oxides in particular are an ideal candidate for suspension spraying as their naturally-occurring particle size is well-suited for suspension preparation. These suspension spray coatings, because of the relatively smaller powder particle size, also result in lower as-sprayed surface roughness and additionally provide the ability to deposit thinner thermal spray coatings [31-32]. Apart from powder particle size, other differences also occur in terms of particle temperature and velocity e.g. between HVOF and APS systems adapted for suspension spraying. Suspension spraying can result in either a truly nanocomposite coating, or a bimodal coating i.e. a lamellar coating with nanostructured zones [1]. In the case of hardmetals these nanostructured zones already occur naturally even in conventional HVOF-sprayed coatings due to rapid solidification of powder particles, however their concentration can be increased by the use of liquid suspensions incorporating nanocomposite powders. A variation of suspension spraying is “solution spraying” where nanosized particles are formed in-flight instead of particles being mixed in the solution in the form of powder [1, 24-25]. Aqueous solution spraying of zirconium, yttrium and aluminum salts, nitrates and other materials have previously been reported [1, 25].

Oberste Berghaus *et al.* [2] conducted a comprehensive study in order to develop WC-12Co nanocomposite coatings by suspension spraying using a commercial APS (AXIAL III, Northwest Mettech Corp., Canada) process with an internal injection module, allowing high in-flight particle velocities up to 800 m/s, but with particle temperatures up to about 2400 °C. Coatings where

prepared mostly from a soft agglomerated powder (60-250 nm nominal carbide grain size, particle sizes < 20 μm) in a 20 wt. % ethanol suspension. Coatings with low porosity showed a maximum hardness of about 700 HV0.3, and showed a pronounced amorphous “hump” in the XRD pattern. When a nanostructured agglomerated and sintered powder in an ethanol/ethylene glycol suspension was used, the crystallinity of the coating and the hardness (about 780 HV0.3) increased. While diffraction peaks of WC were present in the XRD pattern, the formation of metallic tungsten due to strong decarburization was assumed on the base of the position of the maximum of the amorphous “hump”. In order to minimize the carbon loss, relatively lower particle temperatures (below 2200 $^{\circ}\text{C}$), increased particle velocities and the avoidance of the incorporation of highly oxidized overspray into the coating were recommended. They reported that although dense coatings were obtained, the coating quality is compromised by the high temperature and reactivity of small particles.

Detailed recent reviews by Fauchais *et al.* [1,25] discuss some of the advances and technological challenges associated with suspension and solution spraying for a variety of coating materials. Here, specific challenges relating to the stability of the coating process and quality control of deposited coatings are well addressed. Ang and Berndt [26] also recently discussed the role of particle velocities, temperatures and capabilities of different thermal spray systems with a view to comprehend structure-property relationships.

Due to the unique properties of WC as a hard phase and WC-Co as a hardmetal composition [5], as well as the expected improvements due to the use of nanosized WC, there have been significant efforts in research to achieve such nanocomposites. As listed below, there are seven major technological challenges associated with the direct use of nanoparticles such as WC-Co in thermal spraying systems [1-3], which have so far limited the development of WC-Co nanocomposite coatings by spraying with suspensions for industrial applications. The first four can be overcome by the use suspension thermal spraying, whereas the remaining three require careful considerations of suspension composition.

- i.* Direct injection of nanoparticles in thermal spray process cannot be done in conventional conditions due to their lower mass relative to conventional powders.
- ii.* Even if the nanoparticles are injected, they can decompose quickly owing to the high thermal energy imparted due to their smaller size.
- iii.* The atmosphere of thermal spraying can lead to carbon loss in high temperature environments, which can increase due to the small grain size of WC compared to conventional feedstocks.
- iv.* There is generally uneven distribution of nanocomposite particles in spray stream. These challenges can however be somewhat addressed using the suspension feed system and carefully controlling the coating process parameters.
- v.* Suspension development and its feed-mechanism need to be optimized before improved coating quality can be achieved i.e. the high density of WC (15.7 g/cm^3) makes suspension development difficult in comparison to other carbides as it is almost three times the density of TiC (4.93 g/cm^3) and more than twice that of Cr_3C_2 (6.68 g/cm^3).
- vi.* WC-Co can pose specific problems in aqueous suspension as oxides existing at the surface of WC are acidic and that of Co (CoO) are basic in nature [2-3]. This difference in the acidic and alkaline nature can however be avoided by employing a preformed WC-Co composite powder.
- vii.* In aqueous suspensions Co can dissolve which influences the stability of the suspension. The suspension containing these nanoparticles therefore pose complex chemical interactions leading to agglomeration and/or segregation, that could be difficult to control while maintaining the required pH level.

As HVOF is a significantly more appropriate spray process for the manufacturing of WC-Co coatings than APS, it is proposed that S-HVOF represents an alternate spray process that can be used to overcome some of the problems associated with the deposition of nanoparticles, including WC-Co. The preparation of dense oxide ceramic coatings has been successfully demonstrated in the past [10, 30-34]. Second generation HVOF spray guns have been adopted for the use of suspensions, allowing axial injection directly into the burning chamber. This development has been

combined with the development of water-based suspensions with high solids content. The vaporization of water and the resulting cooling effect might be also advantageous for WC-Co coatings. On the other hand the water vapor is a strong oxidizing agent during spraying, but is already present in all HVOF processes due to fuel combustion [35]. In conventional spray processes the surrounding oxygen still provides an additional oxidising environment to the powder particles. Further investigations in this area can clarify the outcome of these two competing processes of cooling and oxidizing environments. The coating process parameters likewise need to be further optimized for the nanocomposite coatings as the powder particle size and its feed mechanism are different from conventional thermal spray coatings.

This paper provides a step forward in the deposition of nanocomposite WC-Co coatings by the use of the S-HVOF process, with a view to investigate their potential for tribological applications. One of the key performance indicators identified in the investigation by Oberste Berghaus *et al.* [2] was the demonstration that an appropriate selection of the process parameters can reduce the thermal loading on nanocomposite powder particles to decrease carbon loss. The current investigation therefore considers the S-HVOF (TopGun) process for coating deposition. A nanostructured WC-Co feedstock powder was selected for this study, the particle size was adapted before suspension preparation by milling. Also the aqueous suspension as indicated above can reduce the thermal load on powder particles e.g. in the investigation by Oberste Berghaus *et al.* [2] ethanol was used. Results of tribomechanical investigations of S-HVOF coatings are compared with conventional HVOF (Jet Kote) coatings. Tribo-mechanical investigations included Scanning Electron Microscopy (SEM), Energy Dispersive X-ray Spectroscopy (EDX), Transmission Electron Microscopy (TEM), X-Ray Diffractometry (XRD), nanohardness and sliding wear evaluations.

2. EXPERIMENTAL

2.1 Coating Deposition

For S-HVOF spraying, an agglomerated and sintered WC-12 wt.% Co spray feedstock powder (Fujimi Corp., Japan - DTS W653-20/5) with sub-micron WC grains as shown in Figure 1(a) was selected as these WC grains are embedded in the metallic matrix, and the majority are thus

protected from the atmosphere during the spray process. This powder has previously been used in cold-spraying of WC-Co coatings [27]. In order to adapt the particle size for suspension preparation, the powder was milled in a planetary ball mill and the resulting nanocomposite powder is shown in Figure 1(b,c).

After milling, the powders were characterized for particle size using a Mastersizer 2000 (Malvern Instruments Ltd.) equipment, as shown in Figure 2a. This measurement characterized the particle size distribution of the powders by laser-light diffraction in the measuring range between 20 nm and 2000 μm . All analysis was conducted in diluted suspension. Prior to analysis the powder was dispersed in liquid by energy input (ultrasound). Sample preparation for powder analysis and measurement itself were done according to ISO 14887:2000 and ISO 13320:2009. The size distribution was calculated from the raw data by Mie theory with a refractive index of 3.5. The viscosity of the suspensions was analyzed prior to spraying (Figure 2b). A Rheometer MCR101 (Anton Paar GmbH) and a DG26.7-SN24833 measuring cup was used for this analysis. The analysis was done at 25 °C in a shear rate range between 50 and 1000 s^{-1} according to DIN 1342-3:2003-11.

Two different suspensions were employed for S-HVOF spraying (labeled as condition # 1 and condition # 2 in Table 1). For condition # 1, aqueous suspensions consisting of 50 wt.% solid content and 50 wt.% deionized water were used. About 1 wt.% (referring to the solid content) of an organic dispersant (polyethylenimine) was added to improve the uniformity and stability of the suspension. Spraying condition # 2 was similar to the spraying condition # 1 except that the content of solids was reduced to 25 wt.%. Figure 2b shows the viscosity variation of both suspensions with the shear rate. S-HVOF spraying was conducted using a modified HVOF (TopGun, GTV mbH, Luckenbach, Germany) spray process using ethene as the fuel gas [10, 30-32]. The construction of the modified torch allows an axial injection of the suspension into the burning chamber. The process parameters were varied in order to achieve long-term stability of the spray process to deposit coatings with low porosity. Different variants were attempted and the coating process parameters used for the coatings used in tribomechanical evaluations reported in this investigation

are summarized in Table 2. In order to ascertain the changes of chemical and phase compositions due to thermal load in the spray process, coating segments detached from the substrate were analyzed for their total carbon content by the combustion method (CS 230, LECO Corporation, St. Joseph, MI, USA) and oxygen content by the carrier gas hot extraction (TCH 600, LECO Corporation, St. Joseph, MI, USA). Selected coatings were also heat treated (Hot Isostatically pressed (HIPed) at 920 °C for 2 hours at 103MPa in inert atmosphere) for transformation of the amorphous constituents into a crystalline state.

In order to compare the performance of nanocomposite S-HVOF coatings with conventional coatings, HVOF (Jet Kote) coatings by means of a WC-12wt.% Co agglomerated and sintered powder were prepared (condition # 3 in Table 1). Industrially optimized coating process parameters were used for the conventional coatings. The fracture response of these conventional HVOF coatings has previously been reported by the authors [36].

All coatings were deposited on AISI440C steel discs of 31 mm diameter and 6 mm thickness. Substrate material for all coatings was grit blasted prior to the coating deposition. The surface of as-deposited coatings was ground and polished prior to tribological wear testing. The coating thickness range for both suspension concentrations is indicated in Table 1.

2.2 Microstructural Evaluations

The microstructure of the powders and coatings was observed via scanning electron microscopy (SEM) by secondary electron (SEI) and backscattered electron (BEI) imaging equipped with energy dispersive x-ray spectroscopy (EDX). These observations were made on the as-sprayed coating surface and also on the polished cross-sections. The chemical compositions of microstructural phases in the powders and coatings were determined via X-ray diffraction (XRD) with Cu-K α radiation (wavelength = 1.5406Å). Transmission electron microscopy (TEM) observations of the samples was made on coating cross-sections prepared initially through mechanical polishing and then by ion milling. The samples were prepared under plane view configuration. They were thinned down to less than 50 μ m by mechanical polishing. The electron transparency was achieved by ion

milling at 5 kV using the GATAN precision ion polisher system (PIPS) at an incidence angle of 5°. The observations were performed on a conventional JEOL 2000 TEM operating at 200 kV.

2.3 Hardness and Modulus Measurements

Vickers microhardness of S-HVOF coatings on polished cross-sections was investigated at two different loads of 0.5 N and 2.94 N. Five measurements were performed at each load. Nanoindentation testing which included hardness and elastic modulus measurements was performed by a calibrated nanoindentation system (NanoTest™ - Micro Materials Limited, UK) equipped with a standard Berkovich nanoindenter. Measurements were taken at room temperature (~23°C) in load control mode at a load of 50 mN. In order to evaluate the load dependency for the smaller carbide size in the S-HVOF coatings, measurements are also presented at 8 mN load for spray conditions # 1 and # 2.

The indentation procedures were programmed as three segments of trapezoidal shape with loading, hold, and unloading segments. A set of six equally spaced measurement sets were performed on the sample cross-sections at various distances from the coating substrate interface. Each measurement set contained five measurements, and averaged values of each measurement set are reported in the results section. The force-displacement ($P-h$) profiles were analyzed using the area function for the Berkovich indenter, which was determined by indentations into fused silica with an elastic modulus of 69.9 GPa. The raw data ($P-h$ profile) were employed to evaluate hardness and reduced elastic modulus (E_r) using the Oliver and Pharr method [37]. The modulus and Poisson's ratio of the diamond indenter was taken as 1140 GPa and 0.07, respectively.

2.4 Sliding Wear Investigations

The sliding wear resistance was examined via ball-on-flat tests. These tests were conducted unlubricated at room temperature on a bench mounted wear test machine (BLR2000M; Bud Labs, USA). The ball-on-flat tests were conducted using AISI 440C steel ball and coated disc sample under a normal load of 25 N. The test conditions were similar to ASTM G133-02 (procedure A), except that the ball radius was slightly larger as 6.35 mm. The lower contact stress due to larger ball

radius was compensated by a longer sliding distance of 500 m. The average surface roughness (R_q) of the disc samples was 0.05 μm . During the test, the disc experienced reciprocating sliding motion at an oscillating frequency of 2.0 Hz, with a stroke length of 10 mm. Five tests were conducted for each test couple. Wear volume loss of the coating was computed from the length of the stroke and the average cross-sectional area of the wear grooves, which was measured via the interferometer (Zygo New View). The corresponding ball volume loss was calculated using the following geometrical relations:

$$V = \frac{\pi H^2}{3}(3R - H), \quad \text{Eq.1}$$

where $H = R - \sqrt{R^2 - r^2}$ and “ R ”, “ r ” are the ball radius and ball-wear-scar radius, respectively. Optical microscopy was used for a precise measurement of the ball-wear-scar radius. This methodology is consistent with the ball volume loss calculations adapted in ASTM G99 and ASTM G133-02. The wear scars and debris after the sliding wear tests were examined by optical and scanning electron microscopy. Friction coefficient was evaluated using a tension-compression load cell mounted on the sliding wear rig. Averaged friction coefficient values and their standard deviation is presented in the results section.

3. RESULTS

3.1 Microstructural Characterization

Figure 3 shows the SEM observations of the S-HVOF and HVOF coatings related to deposition condition # 1, # 2 and # 3 (Table 1). Figure 3(a) shows the surface observation of the as-deposited coating under the deposition condition # 2. Figures 3(b-g) show the cross-section SEM observations of the S-HVOF coatings deposited under deposition conditions # 1 and # 2. Figure 3(h-j) shows the cross-section SEM observation of the conventional HVOF coatings deposited under coating deposition condition # 3. The XRD of milled powder, as-deposited S-HVOF and HIPed coatings are shown in Figure 4a, whereas Figure 4b shows the XRD patterns of the conventional HVOF coating and agglomerated and sintered feedstock powder. The XRD pattern of both S-HVOF coatings shows large amorphous/nanocrystalline “humps”, with a position of the maximum corresponding to metallic tungsten. Peaks of WC and W_2C were also present, the latter with a shift compared to the

standard. The non-metal analysis indicated that for the coating deposited under condition # 2, the carbon and oxygen content was 1.2% and 1.0%, respectively.

For the TEM analysis, the sample configuration after milling indicating the plane view is shown in Figure 5. TEM observations were performed in thin areas near the hole i.e. location 1 is very close to the coating surface, and can be thought to represent TEM observations in the final pass of coating deposition. The results of TEM analysis are presented in the next sections.

3.1.1 TEM Observations of coating for deposition condition # 1

Figure 6 shows the TEM observation of the sample providing the size, morphology and distribution of the particles in the sample. Figure 7 shows the diffraction pattern (DP) from individual particles while in Figure 8 the polycrystalline DP is obtained with a bigger aperture. The d-spacings related to the different rings and the theoretical d-spacings of different possible phases are given in Table 3. The DP from a thicker region of the sample is shown in Figure 9.

3.1.2 TEM Observations of coating for deposition condition # 2

Figure 10 shows the diffraction pattern of particles with different orientations near the sample surface. The d-spacing of these crystals is also shown in this Figure. The diffraction pattern from the marked thick region of the sample is shown in Figure 11. In the thinner region a polycrystalline DP was observed (Figure 12). The d-spacings related to the different rings are given in Table 4.

3.2 Nanomechanical Comparison

Figure 13 indicates the nanoindentation hardness values of coatings considered in this investigation. Values of nanohardness of the selected substrates are also included for comparison. Figure 14 shows the coating and substrate elastic modulus values at the two loads of 50 mN and 8mN. Figure 15 displays the SEM observations of the nanoindents for the coatings deposited using the S-HVOF and conventional HVOF processes. The averaged microhardness values and their standard deviations are shown in Table 1.

3.3 Sliding Wear Tests

Figure 16 illustrates the averaged values of wear volume loss recorded after the sliding wear tests. These values (including the standard deviations) are presented as the ball volume loss, coating volume loss and total volume loss. Averaged friction coefficient values recorded during the sliding wear tests are shown in Figure 17. SEM observations of the wear track at four different magnifications are presented in Figure 18. Wear debris resulting from sliding wear tests are indicated in Figure 19. The SEM analysis of the steel ball surface after the sliding wear tests is shown in Figure 20.

4. DISCUSSION

4.1 Coating Microstructure

The surface morphology of the coating revealed in Figure 3(a) presents fully molten splats with no cracking, indicating thorough heating of the coating particles. SEM micrographs of both suspension sprayed coatings (Fig. 3b-d and 3e-g, respectively) show a low porosity. Comparison of SEM images in Figures 3(c,e) indicate slightly higher relative interlamellar porosity for the 50 wt.% suspension composition (deposition condition # 1), which is attributed to lower thermal load on individual coating particles due to the higher solid particle content in the flame. Comparisons of SEM observations shown in Figures 3(d,g) indicate nanosized particles some of which are consistent with the milled powder particle distribution presented in Figures 1(b,c) and 2(a). The TEM analysis of these nanocomposite particles (Figures 7 and 10) indicated presence of WC and crystalline Co for deposition condition # 1. Similarly WC, W, $\text{Co}_3\text{W}_3\text{C}$ and crystalline Co were observed for the deposition condition # 2. For discussion purpose, these particles in the deposited coating will be collectively termed as “nanosized particles”. These nanosized particles were well distributed within the microstructure, indicating uniform spray conditions for the powder particles in the S-HVOF spray process, as further confirmed by the TEM analysis shown in Figures 6 and 9. The lamella structure displayed in Figure 3(d,g) is also consistent with good wettability and flattening of powder particles on impact. At the coating-substrate interface, the coating follows the profile of grit-blasted substrate with negligible porosity. This is typical of HVOF coatings that

impart higher particle velocity, providing a peening effect in comparison to the plasma spray processes.

One of the main problems associated with the deposition of suspension coatings is the long-term stability of the coating process, as clogging of the spray gun (spitting) can occur [38]. Hence the coating process parameters and suspension composition need to be carefully selected. In this regard the material properties of many oxides such as Al_2O_3 and TiO_2 promote their processing by spraying with suspensions [10,30-32]. Optimisation of suspension and coating process parameters for hardmetals such as WC-Co are significantly more difficult, resulting from the fact that hardware development for S-HVOF spraying was previously focused for processing oxides [31-33]. A number of variants of spray conditions and suspension concentrations were therefore attempted, but only the results of two solution concentrations are indicated here (Table 2). Solid content had an effect on the deposition stability e.g. as the solid content increases, the water content to vaporise per unit volume of the slurry feed rate is lower, this imparts more heat on the powder particles. However, the higher particle concentration per unit volume of flame will reduce the amount of heat transferred. Both of these factors i.e. lower water content increasing heat transfer and higher density of powder particles in the flame reducing heat transfer can result in uneven heating of particles. This can result in vaporisation and condensation of some particles in the spray gun leading to spitting. It was possible to achieve coating thickness in excess of 140 μm for both suspension concentrations, but the suspensions concentration of 25% resulted in this coating thickness without cracks. The internal stresses in the coating after spraying with suspensions concentration of 50% led to cracks in the coating microstructure for thicker coatings.

Comparison of S-HVOF coatings observed in Figures 3(b-g) with conventional HVOF coating shown in Figure 3(h-j) indicates distinctive features. The carbide grain size, which is typically around 3 μm to 5 μm in Figure 3(i-j), is well preserved and distributed in the deposited coating, and is larger than the nanosized particles seen in Figures 3 (d,g).

The XRD comparison of milled powder and deposited coatings provide further insights into the deposition processes during S-HVOF and conventional HVOF spraying. A comparison of the XRD pattern of the feedstock powder and the conventional HVOF coating (Figures 4(a) and 4(b)) indicate sharp WC peaks that are well retained in the coating. This suggests that HVOF process parameters were optimized leading to only a small decarburization, resulting in a lower amount of detectable W_2C (Figure 4b). Contrary to this, the XRD patterns of the S-HVOF coatings indicate some retained WC, W and some W_2C with shifted peak positions, but the pattern is dominated by a large “nanocrystalline peak” between 2θ values of 35 to 48 degrees. The XRD patterns of the milled spray powder shows only tungsten carbide (WC) peaks. Comparison of Figure 4(a) with Figures 4(b) shows that the S-HVOF deposition process led to intensive structural changes in the material. A comparison with the XRD pattern presented by Oberste Berghaus *et al.* [2] shows, that the height of the amorphous/nanocrystalline “hump” is more intensive compared to those of WC. No metallic Co was observed in the S-HVOF or HVOF coatings suggesting that it became part of the amorphous/nanocrystalline matrix. Therefore, an amorphous or nanocrystalline binder phase was produced as observed in Figure 4(a). Crystalline Co was however observed in the TEM analysis (Figures 9 and 11).

The carbon analysis of the coating indicates a more intensive carbon loss than expected, at the same time the oxygen content is also higher than usually observed for WC-Co coatings (typically < 0.2 wt. % [5]). Both W_2C and metallic tungsten are often detected in as-sprayed WC-Co coatings [39], including earlier studies of Verdon *et al.* [40] and Stewart *et al.* [41]. Both studies [40,41] investigated the formation of WC-Co coatings with HVOF spray processes which were identical or comparable with the spray process in the current study, using conventional and nanostructured agglomerated and sintered feedstock powders. Stewart *et al.* [41] have shown that the formation of metallic tungsten depends on the carbide grain size. Thus the higher carbon loss observed in the current study is in agreement with the results of Stewart *et al.* [41] taking into account the feedstock properties and spray conditions. Both studies also proposed mechanisms of W_2C and metallic tungsten formation, which are however different and indicate the need of further research, considering also the results of the current study.

The TEM analysis of the coating sprayed under deposition condition # 1 indicated that near 100nm-wide particles were homogeneously distributed on the whole sample surface (Figure 6). Very few particles were larger than the smallest SAD aperture of the microscope. Figure 7 indicates a diffraction pattern from a single crystal particle. As it can be seen, this particle is WC, which is consistent with the XRD results (Figure 3). The presence of WC on the sample surface observed from the single crystal particle diffraction pattern (Figure 7), was confirmed with the polycrystalline diffraction pattern (Figure 8). Indeed, among the phases in Table 3, only WC has a strong ring 2 as in the experimental diffraction pattern. However the possibility of other phases that may be superimposed to WC cannot be excluded. In the thick part of the sample, individual spots appear in the diffraction pattern (Figure 9). They are likely to be Co grains, which are not detectable by XRD.

The TEM analysis of the coating deposited under deposition condition # 2 indicated approximately 300nm-wide particles as observed on the sample surface (Figure 10). They are identified as W, WC and $\text{Co}_3\text{W}_3\text{C}$ (M_6C). The d-spacings related to the different rings (Figure 12) and the theoretical d-spacings of different possible phases given in Table 4, indicate phases (W, WC, $\text{Co}_3\text{W}_3\text{C}$ and Co) which were already detected with the single crystalline diffraction patterns (Figure 10). However the presence of other superimposed phases like W_2C , $\text{Co}_6\text{W}_6\text{C}$ or $\text{Co}_3\text{W}_9\text{C}_4$ cannot be excluded. In general, both TEM samples were polycrystalline with single crystal particles in the range of 100 nm and 300 nm. For the sample under deposition condition # 1, particles are identified as WC while in coating sample from deposition condition # 2, W, WC and $\text{Co}_3\text{W}_3\text{C}_4$ single crystal particles were observed.

Heating in an inert atmosphere above 600 °C leads to structural changes, bringing the phase composition closer to the equilibrium state, as discussed earlier [5, 39]. The M_6C ($\text{Co}_3\text{W}_3\text{C}$) and M_{12}C ($\text{Co}_6\text{W}_6\text{C}$), the so-called η -phases, are possible equilibrium phases in the W-C-Co system, after loss of carbon in the spray process. Sometimes, their existence in as-sprayed coatings is also reported, as summarized in earlier studies [5, 39]. After the heat treatment at 920 °C WC, metallic tungsten and two η -phases M_6C ($\text{Co}_2\text{W}_4\text{C}$ fit the peaks better than those of $\text{Co}_3\text{W}_3\text{C}$) and M_{12}C

(Co₆W₆C) were observed in the coating. This phase composition confirms the strong carbon loss. However, it should be mentioned that in result of the heat treatment a decrease both of the carbon and oxygen contents is possible, due to internal reduction processes. Previous research by the investigators has shown that heat-treatment of HVOF WC-Co and WC-NiCrBSi coatings can be effectively employed to crystallize amorphous phases and hence further improve the tribomechanical performance of coatings [5-8, 17-19, 39]. This can be also applicable to S-HVOF coatings.

According to the W-C phase diagram [42], W₂C is thermodynamically unstable. Below 1250 °C it can decompose into WC and W during cooling of the WC-Co particle after impact. This decomposition can also result from the heat treatment at 920 °C. Annealing of the coating where Co is present will form the η-phases as mentioned above, and Co can be fully consumed by these reactions. However, any nanoparticles appearing in the as-sprayed coating will strengthen the binder phase and can alter the tribological wear mechanism. Additional studies are needed however to fully understand the microstructure of these nanocomposite hardmetal coatings. In order to meet the challenge to spray hardmetal coatings with suspension, there is a need to develop tailored nanocomposite powders with small carbide grain size, with particle sizes which can formulate stable suspensions. In addition, development of suitable spray equipment which can alter the injection of the suspension to external radial injection can also prove useful in reducing the thermal load on nanocomposite powders.

Although the microstructural features can be further improved by optimizing the coating process parameters and heat-treatment, the presence of nanosized particles can strengthen the metal matrix phase. This can be beneficial under certain tribological conditions e.g. where the wear mechanism is initiated by the preferential wear of metal matrix phase instead of fracture dominated failure of coating. Relatively smaller particle size uniformly distributed in metal matrix is also beneficial under specific tribological conditions. This is mainly due to the fact that in conventional WC-Co coatings, the relatively larger WC particles (Figure 3j) can undergo fracture due to an external load and hence they are dependent on the ability of the Co matrix to arrest the crack and support WC

particle. However, in the case of nanocomposite S-HVOF coatings, the particle size is an order of magnitude smaller (Figures 3d,g). Hence its relatively lower surface area is less likely to undergo fracture as the external load is to be shared between the carbide and metal matrix phase during tribological loading. These microstructural aspects influencing the tribomechanical behavior are further deliberated on in later sections.

In general, low porosity coatings containing nanosized particles were achieved for all deposition conditions considered in this investigation. The SEM observations and XRD analysis above did not indicate that there was any subtle influence of the suspension concentration on the resulting coating microstructure apart from relatively higher interlamellar porosity, and cracking for coating thickness in excess of 140 μm for deposition condition # 1; differences were however observed in the nano-mechanical behavior as discussed in the next section.

4.2 Nanomechanical Response

Nanohardness values of coatings presented in Figure 13 indicate a dependency of averaged hardness values on both the deposition condition and nanoindentation test load. Values of nanohardness measured at the lower load of 8 mN indicate that for coating deposition condition # 1 and # 2, the values are higher than those measured at the 50 mN load. The standard deviation of 8 mN load values is also higher as the reduction in indentation size leads to measurements which can cover either the matrix or carbide phase. SEM images of Berkovich nanoindents shown in Figure 15 at 50 mN load indicate typical indentation diagonal lengths of 1 to 2 μm . At the 8 mN load the indentation diagonal size was submicron and hence the higher values of hardness can be associated with the hardness of carbide particles, whereas the lower values with the metal matrix. In this context the higher values of 20 GPa to 24 GPa can be related to the hardness associated with the carbide particles. The lower values of hardness at a 8 mN load can be related to the hardness of metal matrix phase, where the coatings deposited under deposition condition # 1 show relatively higher values, indicating that more W is present in the metal matrix, as caused by relatively higher overheating of some particles, which also resulted in process instability leading to a lower coating thickness (Table 1). [The presence of WC, W₂C, metallic tungsten and \$\eta\$ - phases was confirmed by](#)

the XRD and TEM analysis. Of all the phases identified the hardness of Co and W will be the lowest (as all other are carbide hard phases). Hence the difference will originate from the relative proportion of W in the nanocomposite matrix.

It is difficult to apply the above analysis of relative changes in carbide and metal matrix hardness to measurements at the higher load of 50 mN, hence only qualitatively analysis of relative changes is discussed (Figures 13 and 14). This is mainly because the ratio of elastic to plastic work during nanoindentation decreases with increasing load, and localized stress contributions from neighboring and underlying carbide or metal matrix phase can no longer be ignored. Similarly, at the higher load of 50 mN, the indentation size ($\approx 3 \mu\text{m}$) was roughly the size of carbide particle in conventional HVOF coatings (Figures 3d and 15a,b). This can lead to carbide fracture as shown in Figure 15b, where arrows indicate the location of carbide fracture, and pop-up of underlying metal matrix phase under indentation load as indicated by arrows in Figure 15a. Qualitatively however, if the higher values of hardness are considered to be associated with the hardness of the carbide, then conventional HVOF coatings deposited under deposition condition # 3 indicate a value of 20 GPa which compares well with the hardness of S-HVOF coatings at 8 mN load (i.e. lower load due to smaller particle carbide size measurement). This is also consistent with the microhardness of coatings shown in Table 1 where both coatings showed similar microhardness. The lower hardness of 5 GPa to 8 GPa for deposition condition # 3 indicates relatively lower values when compared to the S-HVOF coatings (10 GPa to 12 GPa), which is due to a lower content of nanosized phases in the metal matrix of conventional HVOF coatings, and also possibly due to the nanocrystalline phases containing W as discussed earlier. Higher values of metal matrix hardness in S-HVOF coatings are expected to provide more wear resistance and support to the coating microstructure. Lower values of metal matrix hardness in conventional HVOF coatings can be expected to provide relatively higher toughness. Hence the tribological behavior can be expected to be stress dependent.

The SEM observation of the indents at 50 mN load for the S-HVOF coatings (Figures 15c,d) indicate no fracture and the evidence of pop-up was also relatively lower. This is attributed to finer distribution of carbides which leads to sharing of nanoindentation load between the carbide particles

and metal matrix, and higher hardness of the metal matrix. Nanoindentation values at 50 mN load for spray conditions # 1 and # 2 also indicate that the nanohardness values are higher for deposition condition # 2. This is attributed to the fact that at higher solution concentrations, instability in the coating process could result in microstructural zones which are not coherent with the surrounding material. A comparison of nanohardness between loading conditions # 2 and # 3, indicate that the two coatings had similar averaged hardness near the coating surface. However, the S-HVOF coating deposited under deposition condition # 2 shows consistent results throughout the coating thickness. The standard deviation of the averaged values of this coating is also relatively lower than that of conventional HVOF coating. This microstructural and mechanical homogeneity in coatings deposited under deposition condition # 2 altered the wear mechanism as discussed in the next section.

The substrate hardness below 150 μm of the coating substrate interface indicates similar values and their respective standard deviation for all deposition conditions considered in this investigation. However, there is an increase in substrate hardness near the coating substrate interface for the coatings deposited under deposition condition # 2. This change was also observed for deposition condition # 1. This is attributed to relatively higher substrate heating during S-HVOF deposition in comparison to conventional HVOF coatings (deposition condition # 3).

The microhardness values presented in Table 1 also indicate values which are similar for all deposition conditions considered in this investigation. The averaged microhardness ($\text{HV}_{2.9\text{N}}$) values for the S-HVOF coatings (998 ± 73) were higher than those previously reported by Oberste Berghaus *et al.* ($\text{HV}_{0.3} < 800$) [2].

The elastic modulus values of coating presented in Figure 14 indicate through-thickness variations which are similar to the hardness comparison discussed above. Once again, the modulus of coatings deposited under deposition condition # 2 indicates consistent through thickness results with lower standard deviation of averaged values. Based on the hardness and modulus analysis, and the

stability of deposition process under deposition condition # 2, the wear tests were only compared for coatings deposited under deposition conditions # 2 and # 3.

4.3 Sliding Wear Analysis

The total volume loss for the sliding wear test couple which involved S-HVOF coating was on average lower than the conventional HVOF coating, with similar standard deviations for both test couples (Figure 16). The coating volume loss was similar for both S-HVOF and conventional HVOF coatings. The main difference between the two test couples originated from the ball volume loss, which was lower for the S-HVOF coatings. This is attributed to the nanocomposite nature of the carbides in the S-HVOF process, which influenced the three-body abrasive wear process. The contribution of wear originating from the individual carbide and metal matrix phases along with the shape and size of wear debris therefore influenced the tribological process.

4.3.1 Influence of microstructural phases during wear

The calculation of Hertzian contact stress at the start of the wear test under the 25 N load indicate an average and peak value of stress as 1.17 GPa and 4.2 GPa, respectively, with the diameter of point sliding contact as 200 μm . Considering the low surface roughness of coating and ball surface at the start of sliding wear process, the real area of contact will also be similar to 200 μm . This contact stress is shared between the nanosized particles and metal matrix. As the relative carbide size is smaller in S-HVOF coating (Figure 3), the contact stress is more uniformly shared between the metal matrix and nanosized particles. In contrast, the larger carbide size in conventional HVOF coating indicates that the load will be predominantly shared by the carbides due to relatively higher stiffness of WC carbides when compared to Co matrix. As the matrix in conventional HVOF coating is relatively softer (Figure 13), it provides relatively less support in resisting bending deformation of larger carbides under contact load. The bending stress under contact load in smaller carbides will be lower and hence they are less likely to fracture. This leads to a tendency of carbide fracture in conventional HVOF coatings as indicated in Figure 18g.

The metal matrix in conventional HVOF coatings therefore plays a dominant role not only in supporting the carbide network for resisting carbide fracture, but also in mechanically interlocking the carbides due to residual stress [22,43]. This mechanical interlock is caused by the differences in the coefficient of thermal expansion (CTE) of WC or nanosized particles (e.g. CTE of WC between 293 to 1273°K is on average $5.1 \times 10^{-6} \text{ }^\circ\text{K}^{-1}$) and Co (CTE of Co between 293 to 1373°K ranges between $13 \times 10^{-6} \text{ }^\circ\text{K}^{-1}$ to $17 \times 10^{-6} \text{ }^\circ\text{K}^{-1}$). In the S-HVOF coatings the presence of nanocrystalline phase will alter the differential thermal contraction of the microstructural phases, nevertheless it is hypothesized that the smaller carbides will uniformly distribute this stress due to the difference in CTE of different microstructural phases in S-HVOF coatings. This mechanical interlock is of course in addition to the metallurgical bonding between the nanosized particles and surrounding metal matrix.

A harder metal matrix and smaller carbides therefore improves the mechanical integrity in S-HVOF coatings. Due to the nanocomposite nature of S-HVOF coatings the binder mean free path of the metal matrix will be relatively lower [9,20]. This can be observed from Figures 3 and 18. Within the limits of tribological test conditions considered in this investigation, both of these factors of higher hardness and lower mean carbide free path are beneficial to the sliding wear of S-HVOF coatings. This is highlighted in Figures 18(d, h), where preferential wear of the metal matrix phase in conventional HVOF coatings (Figure 18h) has exposed the carbides for erosion and carbide pull-out. In contrast, the nanoparticles in the metal matrix of S-HVOF coatings as shown by dotted circles in Figure 18d, are well supported by the metal matrix and did not display preferential wear of the matrix phase. However, the overall coating volume loss for both S-HVOF and HVOF coatings was similar (Figure 16), this is attributed to that the fact that the S-HVOF coating also contained some larger carbide particles (Fig. 2a), which accelerated the coating wear process. In order to counteract the advantage of metal matrix phase in later stages of wear test, as the role of wear debris shifts the wear mechanism to a combination of two-body and three-body abrasion. It is therefore hypothesized that if the carbide size and WC content in the S-HVOF coatings can be controlled, the coating wear can be further improved. Post-treatment of these nanocomposite coatings may also be beneficial to their tribomechanical properties.

In addition to the differences in carbide fracture and preferential wear of metal matrix phase of conventional HVOF coating, there was one wear mechanism which was similar for both S-HVOF and conventional HVOF coatings. This was the transfer film of steel ball surface adhering to the coating surface as shown in Figures 18 (b,f). The EDX analysis of the transfer film revealed in Figure 18(g) displays preferentially Fe, which confirms the nature of transfer film. The EDX analysis in the Figure of the coating phase indicates W and Co, as expected. The transfer film is expected to be caused by the flash-temperatures at the asperity interactions under the sliding contact load and also via interlocking of debris in the rough coating surface after wear.

4.3.2 Influence of wear debris during wear

The Hertzian contact diameter of 200 μm (area $\approx 0.03 \text{ mm}^2$) at the start of the wear test is expected to grow due to contact conformity caused by the ball and coating wear. This apparent area of contact is approximated as 3 mm^2 at the end of the wear test. The influence of this orders of magnitude increase in apparent area on the contact stress is somewhat reduced due to the role of wear debris. Three body abrasion mechanism caused by wear debris in the contact region therefore dominates the wear in the later stages of the test. As shown in Figure 19, the wear debris was predominantly Fe with WC particles of various shapes and sizes, as indicated by the EDX analysis in Figure 19 (d).

Although the debris was predominantly Fe for both test couples, it is the role of carbide particles in the wear debris which influenced the three body abrasion behavior due to their higher hardness. The nanosized particle debris resulting from the S-HVOF coatings reduced the relative wear of the ball surface. The larger carbides from coating wear of the conventional HVOF coatings therefore resulted in higher overall volume loss of the test couples. These carbides eroded the ball surface as shown in Figure 20, where abrasive marks indicated by arrows show the micro-cutting of ball surface due to carbides. The carbides also dented the ball surface as their irregular shape makes them difficult to roll and slide. These dents are marked by dotted circles in Figure 20. Hence the

bigger carbide size of wear debris increased the ball wear for conventional HVOF coatings as shown in Figure 16.

4.3.3 Influence of contact pairs on frictional behavior

At the start of the wear test, as discussed above in section 4.3.1, there was preferential contact between the steel ball surface and the larger WC carbides of the conventional HVOF coatings. This WC to metal contact reduced the surface interaction in comparison to e.g. metal to metal contact, which lead to lower friction coefficient in the early stages of wear tests for conventional HVOF coatings (up to 100m sliding distance), as indicated in Figure 17a. During the later stages of the wear tests however, the frictional coefficient was more dominated by the role of wear debris. Just like the strong influence of carbide shape and size in wear debris on the ball wear, the nanosized particles in the wear debris of S-HVOF coating couples also lead to a lower average friction coefficient in later stages of the wear tests. This is indicated in Figure 17a for sliding distances in excess of 100m, and also in Figure 17b, which displays the steady state average friction values for both test couples.

5. CONCLUSIONS

- 1) Nanostructured coatings with low porosity and hardness up to 1000 HV0.3 have been deposited by S-HVOF using an aqueous suspension of a milled nanostructured WC-Co feedstock. The microstructure of S-HVOF coatings indicates nanosized particles (WC, W, M_6C , $M_{12}C$) some of which were inherited from the milled powder whereas others formed as a result of carbon loss, demonstrating that the S-HVOF process retained the nanocomposite features during coating deposition.
- 2) TEM investigations indicated nanosized particles in the range of 100nm to 300nm. These particles were identified as W, WC and Co_3W_3C . In addition the presence of crystalline Co was detected in the TEM analysis.
- 3) A comparison of S-HVOF and conventional HVOF coatings points toward phase transformations occurring in the S-HVOF coating process which led to nanostructured and

amorphous phases. This phase transformation in the conventional HVOF coatings was relatively lower.

- 4) After the heat treatment at 920 °C WC, metallic tungsten and two η -phases M_6C (Co_2W_4C) and $M_{12}C$ (Co_6W_6C) were observed in the coating.
- 5) Sliding wear evaluations indicated that the test couples for S-HVOF coatings had a relatively lower averaged volume loss in comparison to the conventional HVOF coatings. A similar trend was observed for the averaged friction coefficient values.
- 6) Three body abrasion mechanism caused by the wear debris was also different between the S-HVOF and conventional HVOF coatings. A smaller and more uniformly distributed nanosized particle structure in the S-HVOF coatings provided better support for the metal matrix. There was preferential abrasion of metal matrix in the conventional HVOF coatings.
- 7) The wear mechanism was dominated by three-body abrasion caused by the pull-out of carbides from the coatings. As the S-HVOF coatings had relatively smaller particle size it resulted in lower ball wear volume loss.
- 8) Solid content of the aqueous solution and nanoindentation test load in S-HVOF spraying had a direct influence on the elastic modulus and hardness values. S-HVOF coatings deposited under deposition condition # 2 had a higher, and more uniform through thickness averaged values when compared to the conventional coatings.

6. ACKNOWLEDGEMENT

Authors acknowledge the support of Youssef Elakwah at Alfaisal University KSA in conducting the nano-indentation experiments. Irina Shakhverdova (Fraunhofer IWS) is thanked for support in evaluation of XRD pattern. Financial support of Saudi Aramco for the research project is also gratefully acknowledged.

7. REFERENCES

- [1] P. Fauchais, G. Montavon, R.S. Lima, and B.R. Marple, Engineering a New Class of Thermal Spray Nano-based Microstructures from Agglomerated Nanostructured Particles,

Suspension and Solutions: An Invited Review, *Journal of Physics D: Applied Physics*, 2011, 44, art no. 093001 (53 pp).

- [2] J. Oberste Berghaus, B. Marple, and C. Moreau, Suspension Plasma Spraying of Nanostructured WC-12Co Coatings, *Journal of Thermal Spray Technology*, 2006, 15, p 676-681
- [3] V. Chawla, B.S. Sidhu, D. Puri, and S. Prakash, State of Art: Plasma Sprayed Nanostructured Coatings: A Review, *Materials Forum*, 2008, 32, p 137-143
- [4] Z.Z. Fang, X. Wang, T. Ryu, K.S. Hwang, and H.Y. Sohn, Synthesis, Sintering, and Mechanical Properties of Nanocrystalline Cemented- A Review, *International Journal of Refractory Metals & Hard Materials*, 2009, 27, p 288-299
- [5] L.-M. Berger, in: *Comprehensive Hard Materials, Volume 1, Hardmetals*, V. Sarin, D. Mari, L. Llanes, C. Nebel (eds), Elsevier, Amsterdam, 2014, p 479-514
- [6] V. Stoica, R. Ahmed, T. Itsukaichi, and S. Tobe, Sliding Wear Evaluation of HIPed Thermal Spray Cermet Coatings, *Wear*, 2004, 257(11), p 1103-1124
- [7] S. Stewart, R. Ahmed, and T. Itsukaichi, Rolling Contact Fatigue of Post-treated WC-NiCrBSi Thermal Spray Coatings, *Surface and Coatings Technology*, 2005, 190(2-3), p 171-189
- [8] R. Ahmed, and M. Hadfield, Mechanisms of Fatigue Failure in Thermal Spray Coatings, *Journal of Thermal Spray Technology*, 2002, 11(3), p 333-349
- [9] Š. Houdková, F. Zahálka, M. Kašparová, and L.-M. Berger, Comparative Study of Thermally Sprayed Coatings Under Different Types of Wear Conditions for Hard Chromium Replacement, *Tribology Letters*, 2011, 43, p 139-154
- [10] F.-L. Toma, L.-M. Berger, C.C. Stahr, T. Naumann, and S. Langner, Microstructures and Functional Properties of Suspension-Sprayed Al₂O₃ and TiO₂ Coatings: An Overview, *Journal of Thermal Spray Technology*, 2010, 19(1-2) , p 262-274
- [11] V. Bonache, M.D. Salvador, J.C. García, E. Sánchez, and E. Bannier, Influence of Plasma Intensity on Wear and Erosion Resistance of Conventional and Nanometric WC-Co Coatings Deposited by APS, *Journal of Thermal Spray Technology*, 2011, 20(3), p 549-559

- [12] E. Sánchez, E. Bannier, M.D. Salvador, V. Bonache, J.C. García, J. Morgiel, and J. Grzonka, Microstructure and Wear Behavior of Conventional and Nanostructured Plasma-Sprayed WC-Co Coatings, *Journal of Thermal Spray Technology*, 2010, 19(5), p 964-974
- [13] G. Bolelli, V. Cannillo, L. Lusvardi, R. Rosa, A.V. Wanhuk, B. Choib, R. Dey, C. Weyant, S. Sampath, Functionally Graded WC-Co/NiAl HVOF Coatings for Damage Tolerance, *Wear and Corrosion Protection, Surface and Coatings Technology*, 2012, 206(8-9), p 2585-2601
- [14] H. Chen, G. Gou, M. Tu, and Y. Liu, Research on the Friction and Wear Behavior at Elevated Temperature of Plasma-Sprayed Nanostructured WC-Co Coatings, *Journal of Materials Engineering and Performance*, 2010, 19(1), p 1-6
- [15] H.L. de Villiers Lovelock, Powder/Processing/Structure Relationship in WC-Co Thermal Spray Coatings: A Review of the Published Literature, *Journal of Thermal Spray Technology*, 1998, 7(3), pp 357-373
- [16] S. Stewart, and R. Ahmed, Contact Fatigue Failure Modes in Hot Isostatically Pressed WC-12%Co Coatings, *Surface and Coatings Technology*, 2003, 172, p 204-216
- [17] V. Stoica, and R. Ahmed, Influence of Vacuum Heat Treatment on Sliding Wear of Thermal Spray Cermet Coatings, *Surface and Coating Technology*, 2005, 199(1), p 7-21
- [18] V. Stoica, R. Ahmed, T. Itsukaichi, and S. Tobe, Sliding Wear Evaluation of Hot Isostatically Pressed (HIPed) Thermal Spray Cermet Coatings, *Wear*, 2004, 257(11), p 1103-1124
- [19] V. Stoica, R. Ahmed, and S. Tobe, Wear of Hot Isostatically Pressed (HIPed) Thermal Spray Cermet Coatings, *Journal of Thermal Spray Technology*, 2004, 13(1), p 93-107
- [20] P. Chivavibul, M. Watanabe, S. Kuroda, and K. Shinoda, Effects of Carbide Size and Co Content on the Microstructure and Mechanical Properties of HVOF-Sprayed WC-Co Coatings, *Surface & Coatings Technology*, 2007, 202, p 509-521
- [21] J. He, and J.M. Schoenung, Review-Nanostructured Coatings, *Materials Science and Engineering A*, 2002, 336, p 274-319
- [22] R. Ahmed, N.H. Faisal, A.M. Paradowska, M.E. Fitzpatrick, and K.A. Khor, Neutron diffraction residual strain measurements in nanostructured hydroxyapatite coatings for

- orthopaedic implants, *Journal of Mechanical Behavior of Biomaterials*, 2011, 4(8), p 2043-2054
- [23] F. Tarasi, "Suspension Plasma Sprayed Alumina-Yttria Stabilized Zirconia Nanocomposite Thermal Barrier Coatings-Formation and Roles of the Amorphous Phase," Ph.D. Thesis, Concordia University, 2010
- [24] P. Fauchais, G. Montavon, Latest Developments in Suspension and Liquid Precursor Thermal Spraying, 2010, 19(1-2), p 226–239
- [25] P. Fauchais, A. Vardelle, Innovative and Emerging Processes in Plasma Spraying: From Micro-to Nanostructured Coatings, *Journal of Physics D: Applied Physics*, 2011, 44, art no. 194011 (14pp)
- [26] A.S.M. Ang, C.C. Berndt, A Review of Testing Methods for Thermal Spray Coatings, *Int. Mater. Rev.* 2014, 59 (4), 179-223.
- [27] M. Couto, S. Dosta, M. Torrell, J. Fernández, and J.M. Guilemany, Cold Spray Deposition of WC-17 and 12Co Cermets onto Aluminum, *Surface and Coatings Technology*, 2013, 235, p 54-61
- [28] J. M. Guilemany, S. Dosta, J. Nin, and J. R. Miguel, Study of the Properties of WC-Co Nanostructured Coatings Sprayed by High-Velocity Oxy Fuel, *Journal of Thermal Spray Technology*, 2005, 14, p 405-413
- [29] Z.-G. Ban, and L.L. Shaw, Characterization of Thermal Sprayed Nanostructured WC-Co Coatings Derived from Nanocrystalline WC-18wt.%Co Powders, *Journal of Thermal Spray Technology*, 2003, 12, p 112-119
- [30] F.-L. Toma, L.-M. Berger, S. Scheitz, S. Langner, C. Rödel, A. Potthoff, V. Sauchuk, and M. Kusnezoff, Comparison of the Microstructural Characteristics and Electrical Properties of Thermally Sprayed Al₂O₃ Coatings from Aqueous Suspensions and Feedstock Powders, *Journal of Thermal Spray Technology*, 2012, 21(3-4), p 480-488
- [31] L.-M. Berger, F.-L. Toma, and A. Potthoff, Thermal Spraying with Suspensions-An Economic Spray Process, *Thermal Spray Bulletin*, 2013, 6(2) p 98-101
- [32] F.-L. Toma, L.-M. Berger, S. Langner, and T. Naumann, Suspension Spraying-The Potential of a New Spray Technology, *Thermal Spray Bulletin*, 2010, 3(1), p 24-29.

- [33] A. Killinger, M. Kuhn, R. Gadow, High-Velocity Suspension Flame Spraying (HVSFS), a New Approach for Spraying Nanoparticles with Hypersonic Speed, *Surf. Coat. Technol.*, 2006, 201 (5), 1922-1929.
- [34] A. Killinger, R. Gadow, A. Rempp, A. Manzat, Advanced Ceramic Tribological Layers by Thermal Spray Routes, *Adv. Sci. Technol.*, 2010, 66, 106-119.
- [35] K. Korpiola, High Temperature Oxidation of Metal, Alloy and Cermet Powders in HVOF Spraying Process, Dissertation, Helsinki University of Technology, 2006.
- [36] N. H. Faisal, J. A. Steel, R. Ahmed and R. L. Reuben, The Use of Acoustic Emission (AE) to Characterise Vickers Indentation Behaviour of HVOF Thermally Sprayed WC-12%Co Coatings, *Journal of Thermal Spray Technology*, 2009, 18(4), p 525-535
- [37] W.C. Oliver, and G. M. Pharr, An Improved Technique for Determining Hardness and Elastic Modulus Using Load and Displacement Sensing Indentation Experiments, *Journal of Materials Research*, 1992, 7, p 1564-1583.
- [38] S. Osawa, T. Itsukaichi and R. Ahmed, "Influence of Powder Size and Strength on HVOF Spraying - Mapping the Onset of Spitting", *Advancing the Science and Applying the Technology*, International Thermal Spray Conference, Florida, USA, pp. 819-824, 2003.
- [39] S. Thiele, K. Sempf, K. Jaenicke-Roessler, L.-M. Berger, and J. Spatzier, Thermophysical and Microstructural Studies on Thermally Sprayed Tungsten Carbide-Cobalt Coatings, *Journal of Thermal Spray Technology*, 2011, 20(1-2), p 358-365
- [40] C. Verdon, A. Karimi, J.-L. Martin, A Study of High Velocity Oxy-Fuel Thermally Sprayed Tungsten Carbide Based Coatings. Part 1: Microstructures, *Mater. Sci. Engineer.* 1998, A246 (1-2), 11-24.
- [41] D.A. Stewart, P.H. Shipway, D.G. McCartney, Microstructural Evolution in Thermally Sprayed WC-Co Coatings: Comparison between Nanocomposite and Conventional Starting Powders, *Acta Mater.*, 2000, 48 (7), 1593-1604.
- [42] A.S. Kurlov, and A.I. Gusev, Tungsten Carbides and W-C phase diagram, *Neorganicheskie Materialy*, 2006, 42(2), p 156-163, in Russian [*Inorganic Materials*, 2006, 42(2), p 121-127, in English].

- [43] R. Ahmed, H. Yu, L. Edwards and J. Santisteban, “Neutron Diffraction Residual Strain Measurements in Post-treated Thermal Spray Cermet Coatings”, *Material Science and Engineering-A*, Vol. 498, pp. 191-202, 2008.

FIGURES AND TABLES

Table 1, Spray conditions

Spray Condition	Suspension Concentration	Spray Process	Coating thickness	Microhardness	
				HV _{0.5N}	HV _{2.9N}
Condition # 1	50 wt.% solids in aqueous suspension	S-HVOF (TopGun)	≈ 75 to 140 μm	957 ± 105	-
Condition # 2	25 wt.% solids in aqueous suspension	S-HVOF (TopGun)	≈ 140 to 250 μm	991 ± 79	998 ± 73
Condition # 3	Conventional agglomerated and sintered powder spraying.	HVOF (Jet Kote)	≈ 330 μm	-	924 ± 127

Table 2, Spray Parameters for S-HVOF coatings

Spray Condition	Process parameters		
	C ₂ H ₄ (l/min)	O ₂ (l/min)	Spray distance (mm)
Condition # 1	75	170	80
Condition # 2	75	170	90

Table 3: Experimental d-spacing measured from the different rings and theoretical d-spacing for some possible phases for deposition condition # 1. In brackets are the hkl values. The intensities of the x-ray reflections are also indicated in the table.

Ring number	d_{exp} (Å)	d_{th} (Å)						
		WC (Hex.)	W ₂ C (Hex.)	W (Cubic)	Co ₃ W ₃ C (Cubic)	Co ₆ W ₆ C (Cubic)	Co ₃ W ₉ C ₄ (Hex.)	Co (Hex.)
1	2.2	-	2.3 (-1-11) Int100	2.2 (011) Int100	2.1 (511) Int100	2.1 (511) Int100	2.2 (301) Int100	2.2 (010) Int100
2	1.9 (Strong)	1.9 (101) Int83	-	-	1.9 (440) Int40	1.9 (440) Int35	1.9 (302) Int10	1.9 (002) Int25
3	1.7	-	1.7 (-1-12) Int15	1.6 (002) Int17	1.7 (620) Int2	-	1.7 (400) Int11	-
4	1.4 (Weak)	1.4 (002) Int5	1.5 (300) Int16		1.4 (731) Int12	1.4 (731) Int15	1.4 (205) Int54	1.5 (012) Int13
5	1.1	1.2 (201) Int11	1.1 (-2-22) Int3	1.1 (022) Int12	1.1 (755) Int13	-	1.1 (325) Int8	1.2 (013) Int16

Table 4: Experimental d-spacing measured from the different rings in DP1 and theoretical d-spacing for some possible phases for deposition condition # 2. In brackets are the hkl values. The intensities of the x-ray reflections are also indicated in the table.

Ring number	d_{exp} (Å)	d_{th} (Å)						
		WC (Hex.)	W ₂ C (Hex.)	W (Cubic)	Co ₃ W ₃ C (Cubic)	Co ₆ W ₆ C (Cubic)	Co ₃ W ₉ C ₄ (Hex.)	Co (Hex.)
1	2.2 (W)	-	2.3 (-1-11) Int100	2.2 (011) Int100	2.1 (511) Int100	2.1 (511) Int100	2.2 (301) Int100	2.2 (010) Int100
2	1.9 (S)	1.9 (101) Int83	-	-	1.9 (440) Int40	1.9 (440) Int35	1.9 (302) Int10	1.9 (002) Int25
3	1.7	-	1.7 (-1-12) Int15	1.6 (002) Int17	1.7 (620) Int2	-	1.7 (400) Int11	-
4	1.2	1.2 (201) Int11	1.1 (-2-22) Int3	1.1 (022) Int12	1.1 (755) Int13	-	1.1 (325) Int8	1.2 (013) Int16

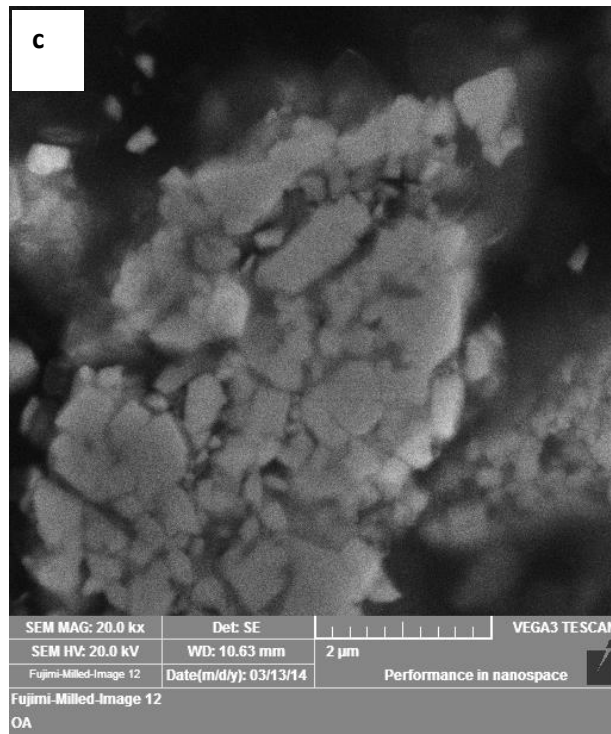
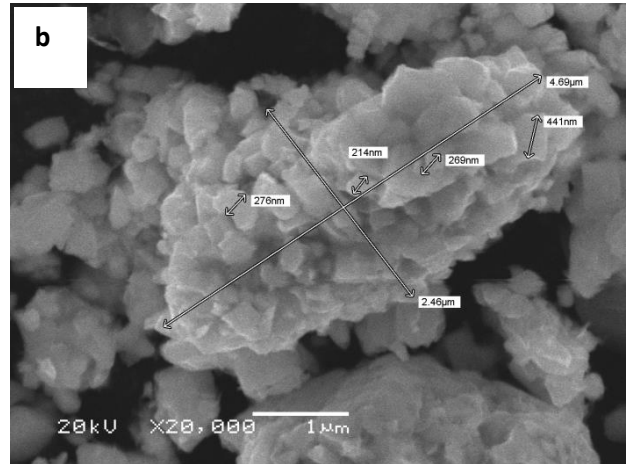
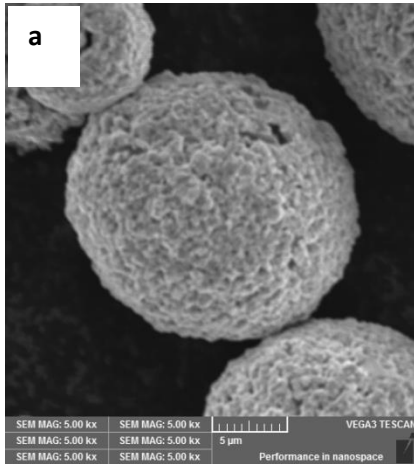
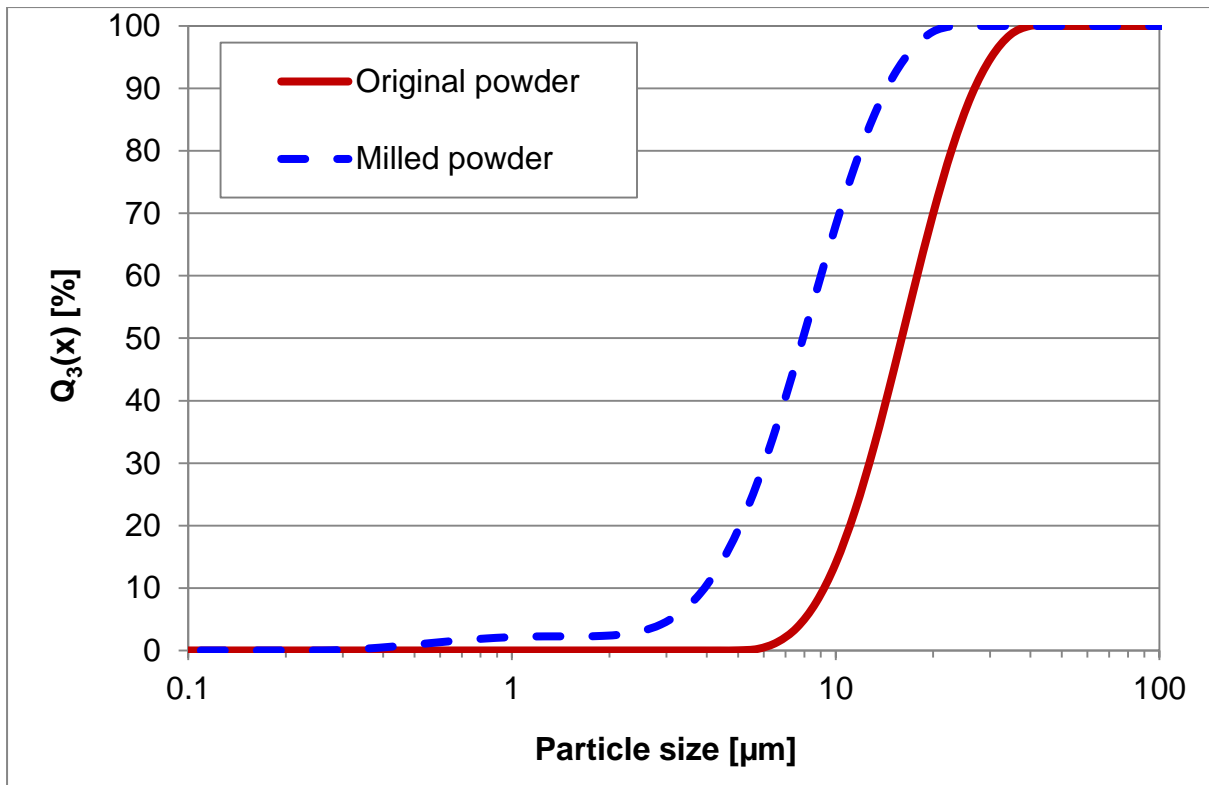
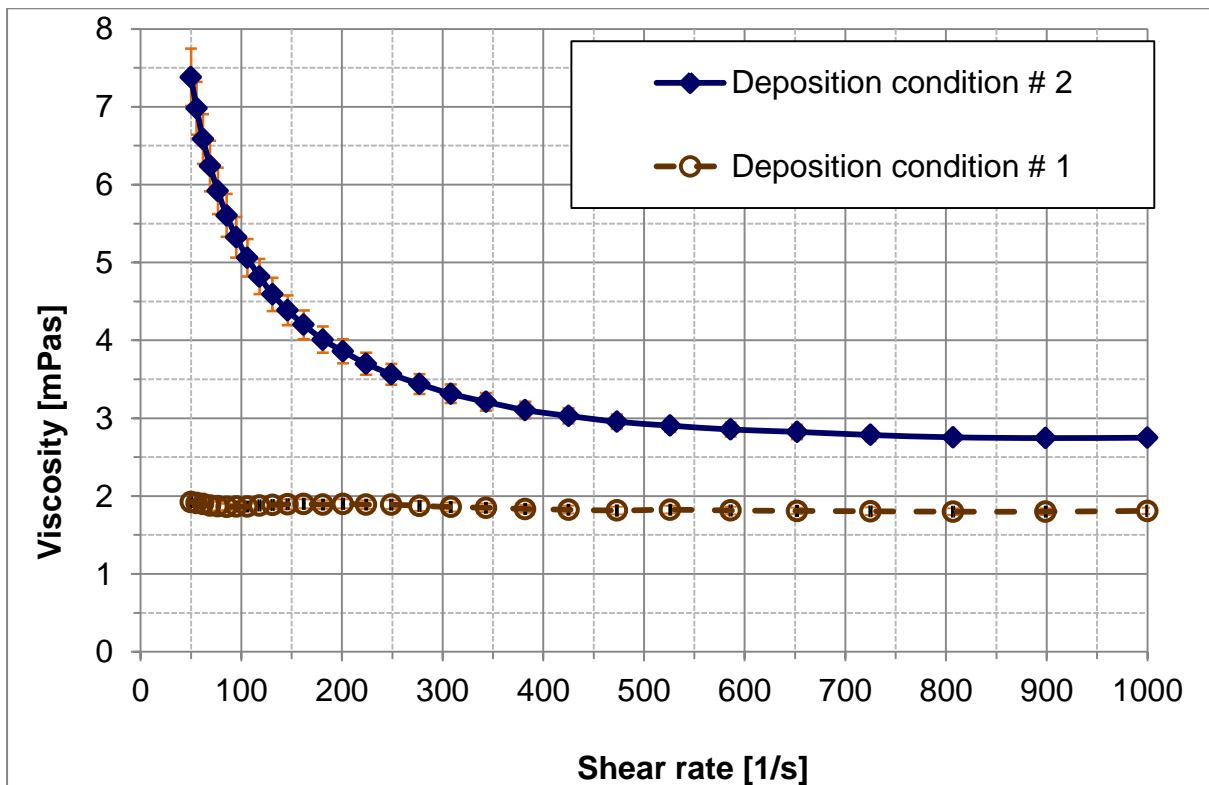


Figure 1, SEM observations of the a) agglomerated and sintered WC-12 wt.% Co spray powder, b) nano-structured powder after milling, c) cross-section of milled powder.

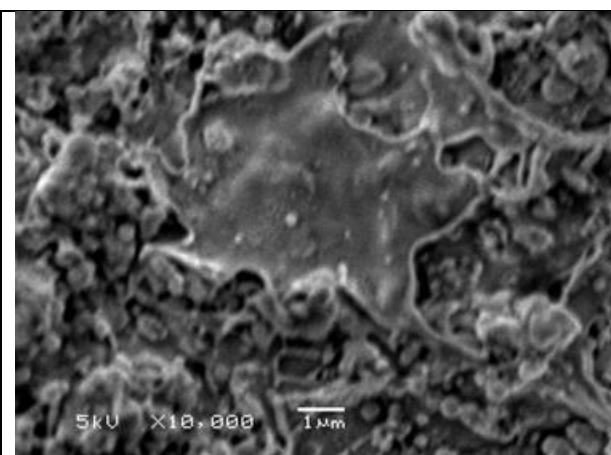


a)

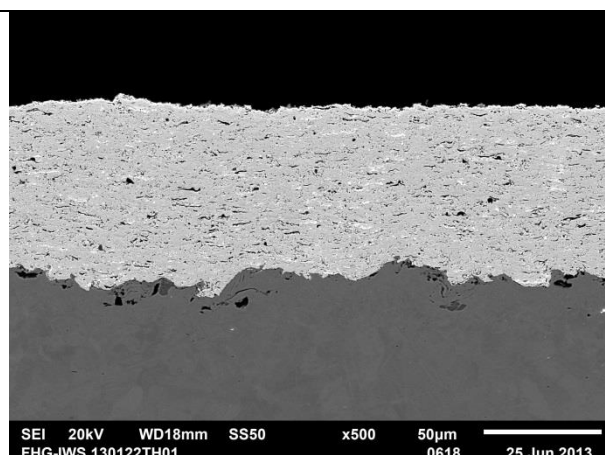


b)

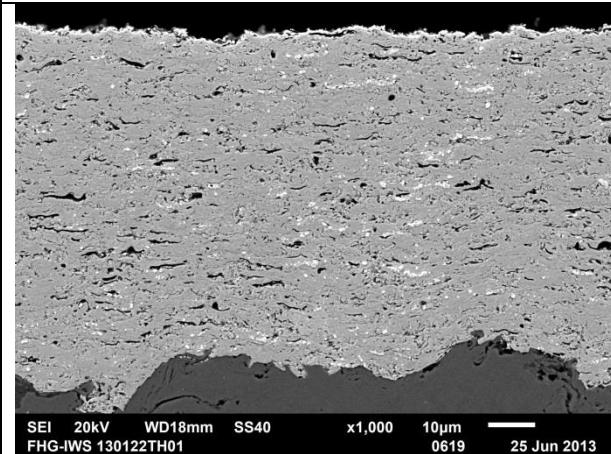
Figure 2, a) Powder size distribution of original and milled powder, b) Viscosity and shear rate measurements of the aqueous concentrations for spray conditions # 1, 2.



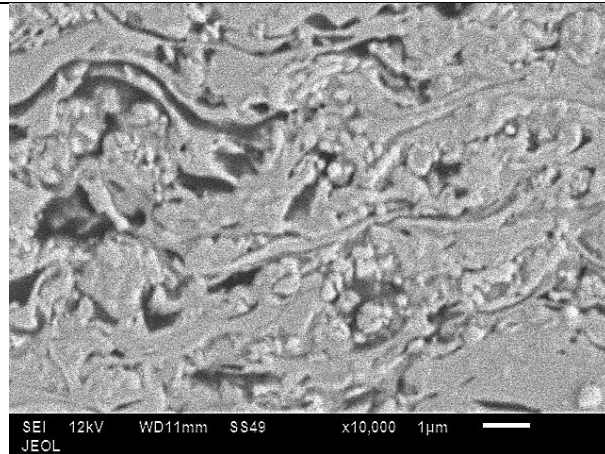
a)



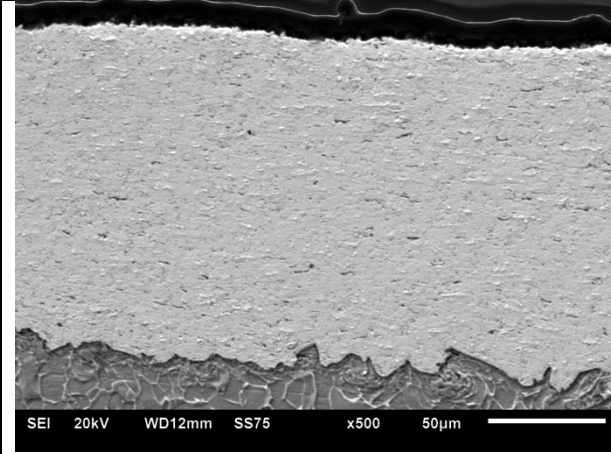
b)



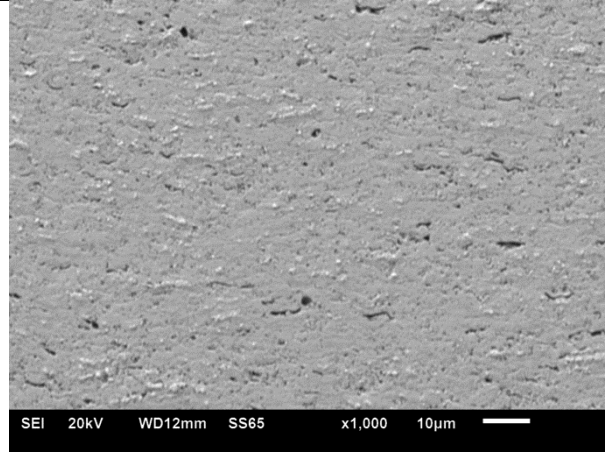
c)



d)



e)



f)

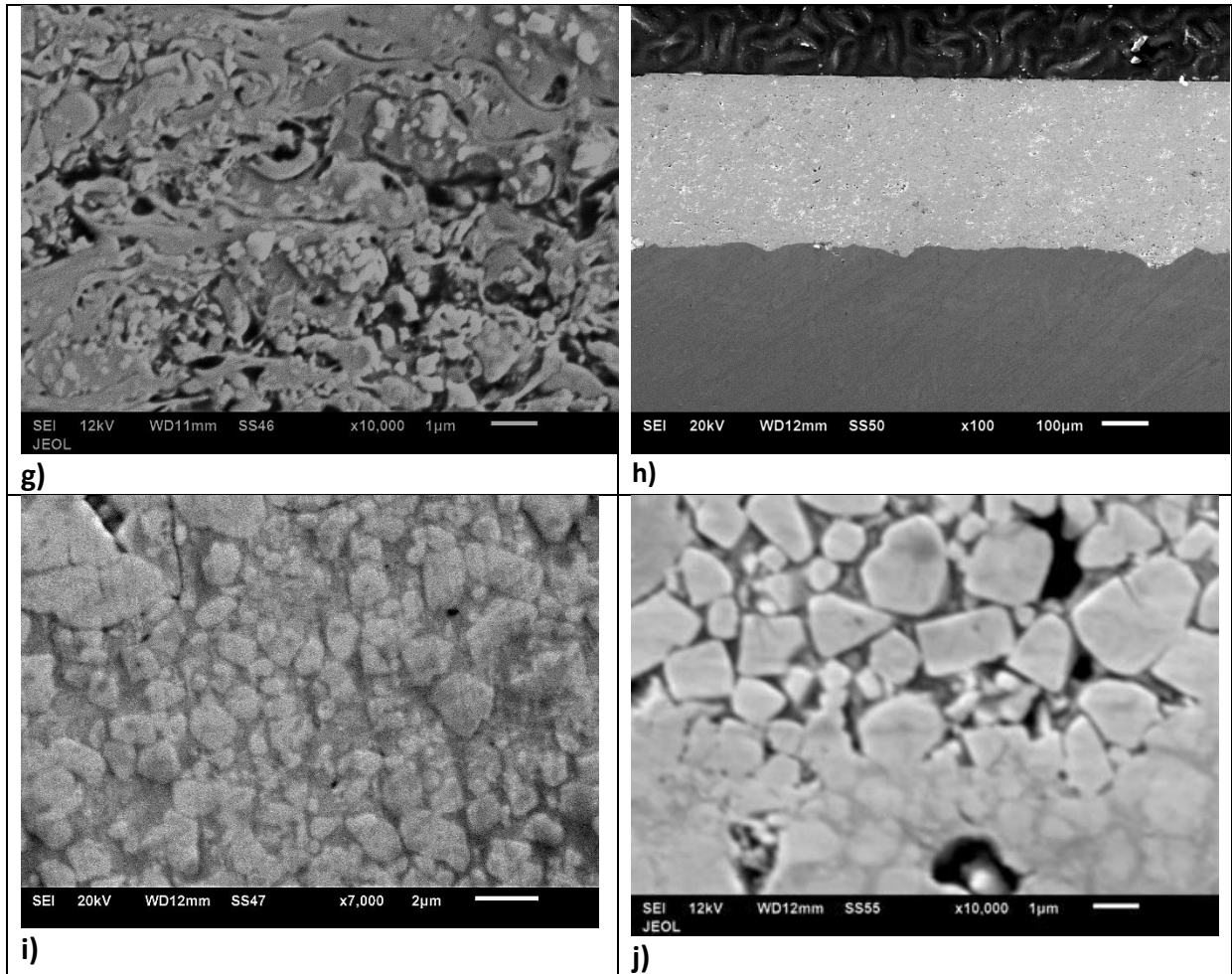
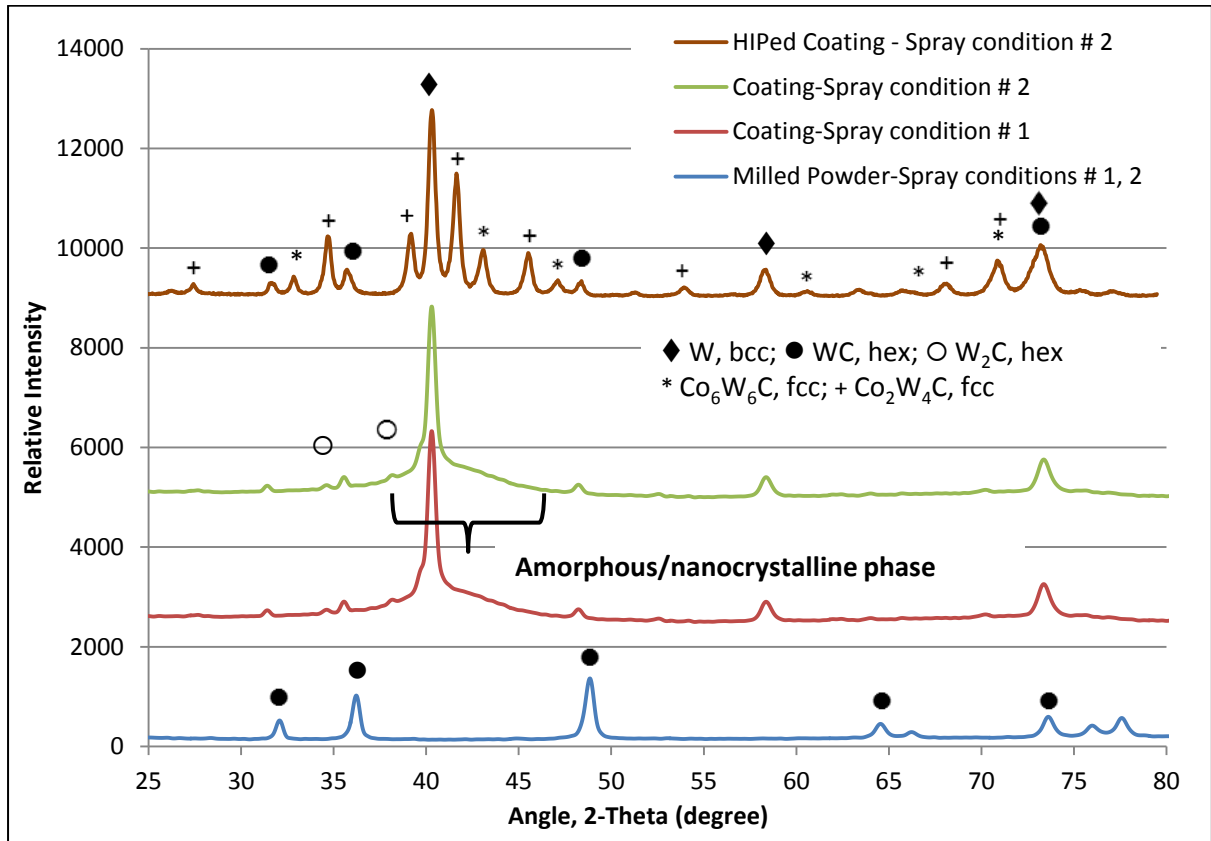
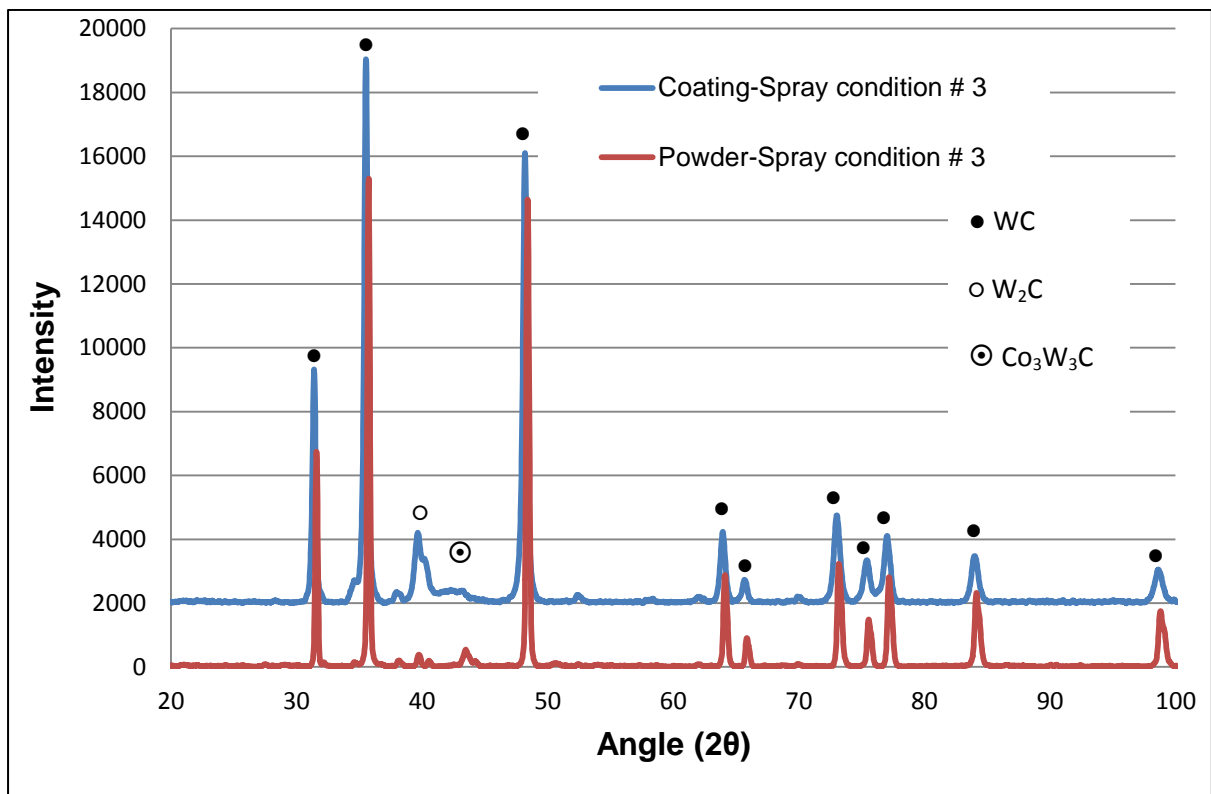


Figure 3, SEM observations of deposited coatings, a) surface of as-deposited coatings under spraying condition # 2, b,c,d) cross-section observation of coating deposited under spray condition # 1, e,f,g) cross-section observation of coating deposited under spray condition # 2, h,i,j) cross-section observation of coating deposited under spray condition # 3.



a)



b)

Figure 4, XRD pattern of spray powder and coating for deposition conditions # a) 1, 2 and b) 3.

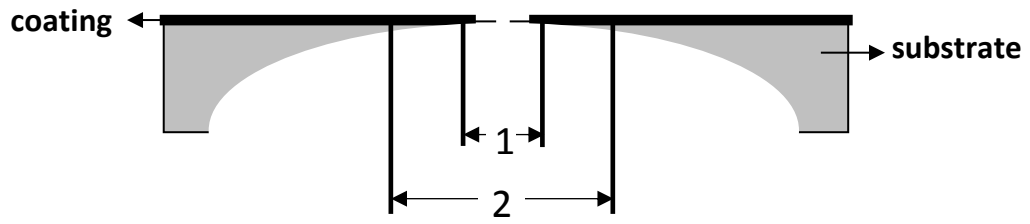


Figure 5, Representation of a plane view TEM sample configuration.

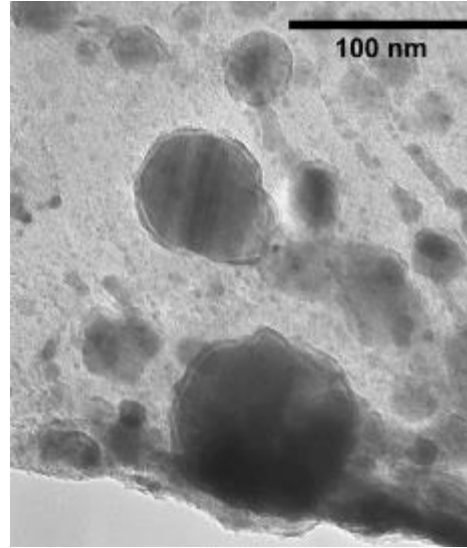
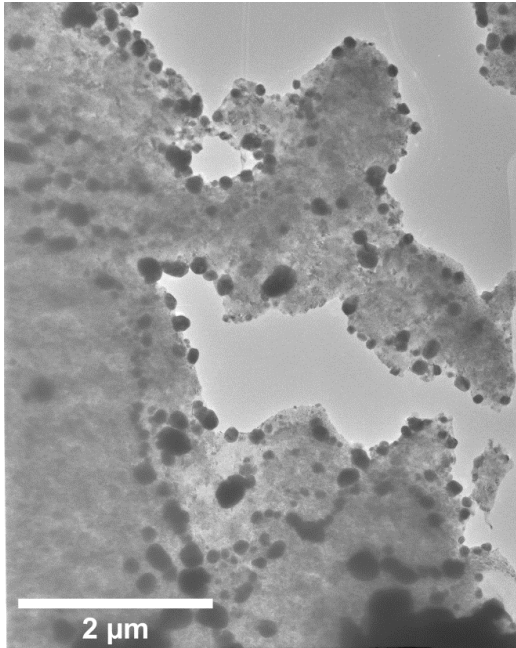
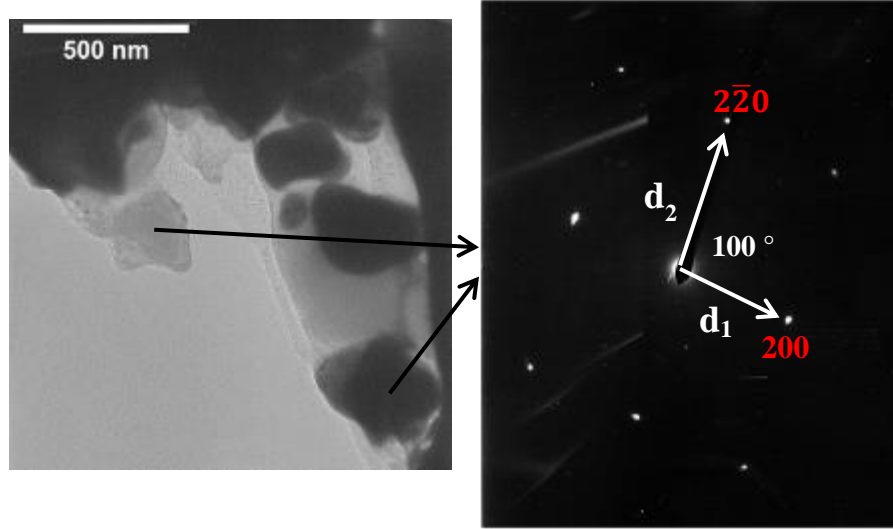


Figure 6: Plane view image of the sample coated under deposition condition # 1.



WC $d_1 = d_{200} = 1.3 \text{ \AA}$, $d_2 = d_{2-20} = 1.0 \text{ \AA}$
 $2-20 \wedge 200 = 100^\circ$

Figure 7: Experimental diffraction pattern (DP) from a particle coated under deposition condition # 1. The DP matches with WC.

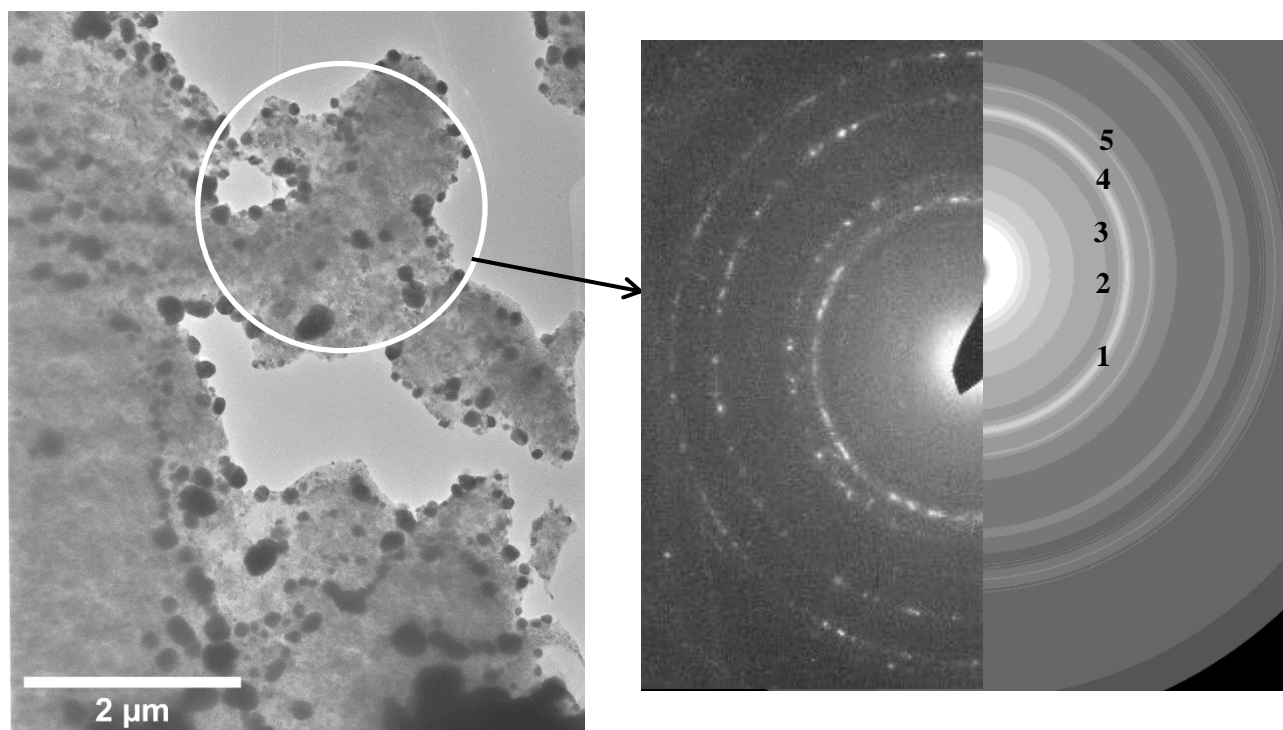
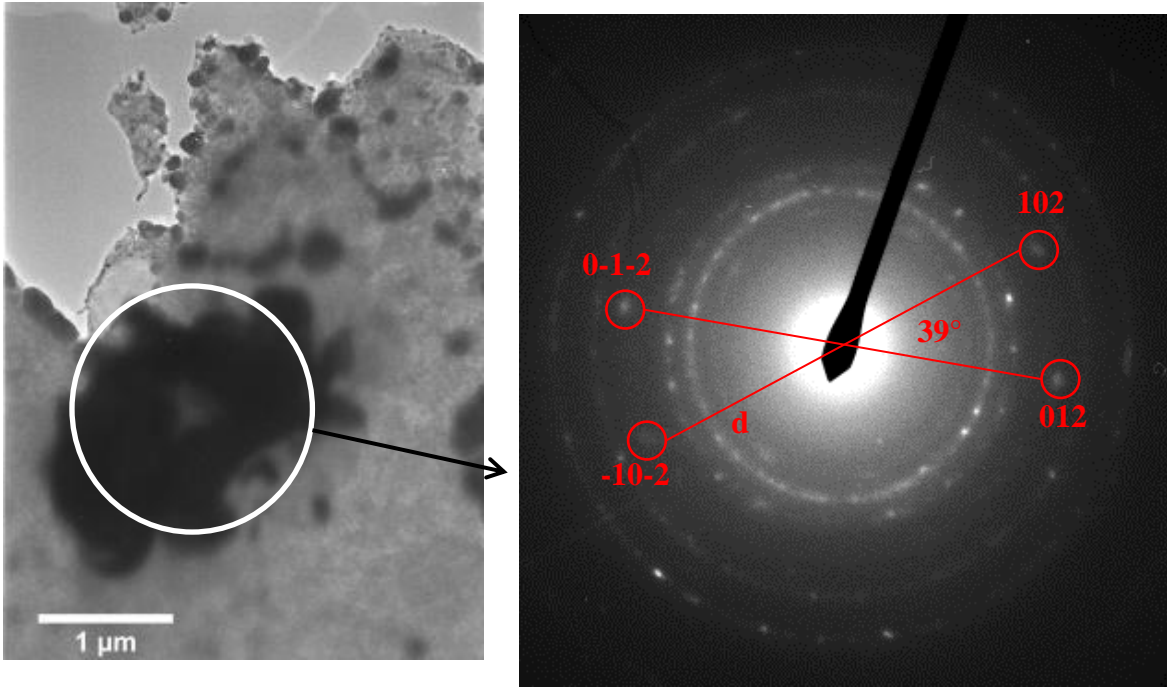


Figure 8: Diffraction pattern of coated sample under deposition condition # 1 plane view sample.



Co, $d=1.5 \text{ \AA}$

Figure 9: Observation of diffraction pattern from a thick region of the sample coated under deposition condition # 1: apparition of new diffraction spots probably linked to Co.

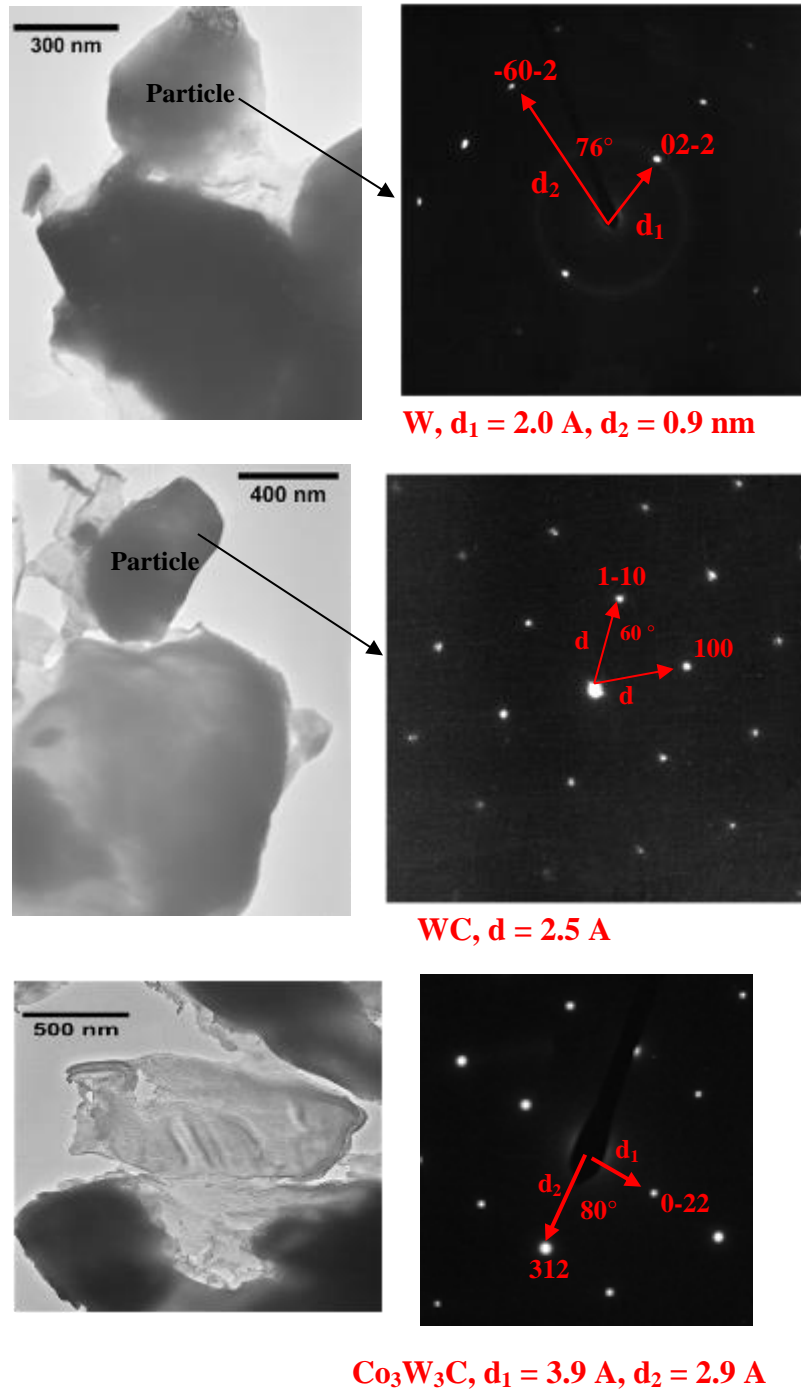


Figure 10: Observation of single crystal oxide particles with different orientations for coated sample under deposition condition # 2. They are identified as W, WC and $\text{Co}_3\text{W}_3\text{C}$.

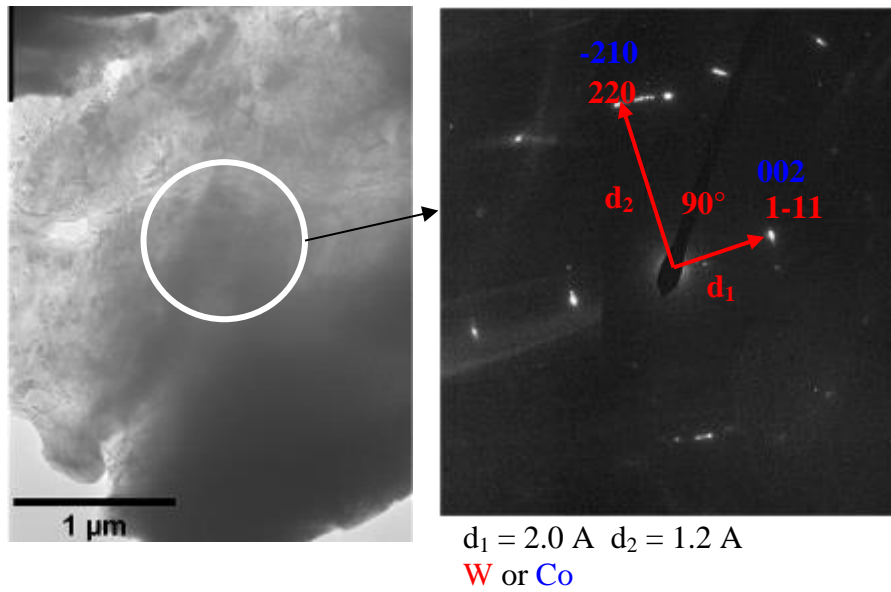


Figure 11: Near single crystalline diffraction pattern from the thick region of the sample coated under deposition condition # 2. The DP may be linked to W and/or Co.

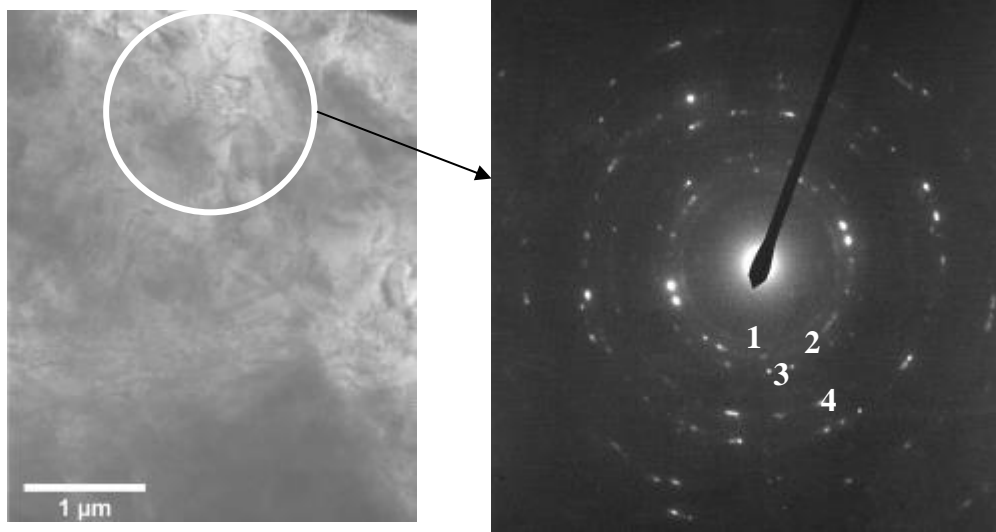


Figure 12: Diffraction pattern from a thin region of the sample coated under deposition condition # 2.

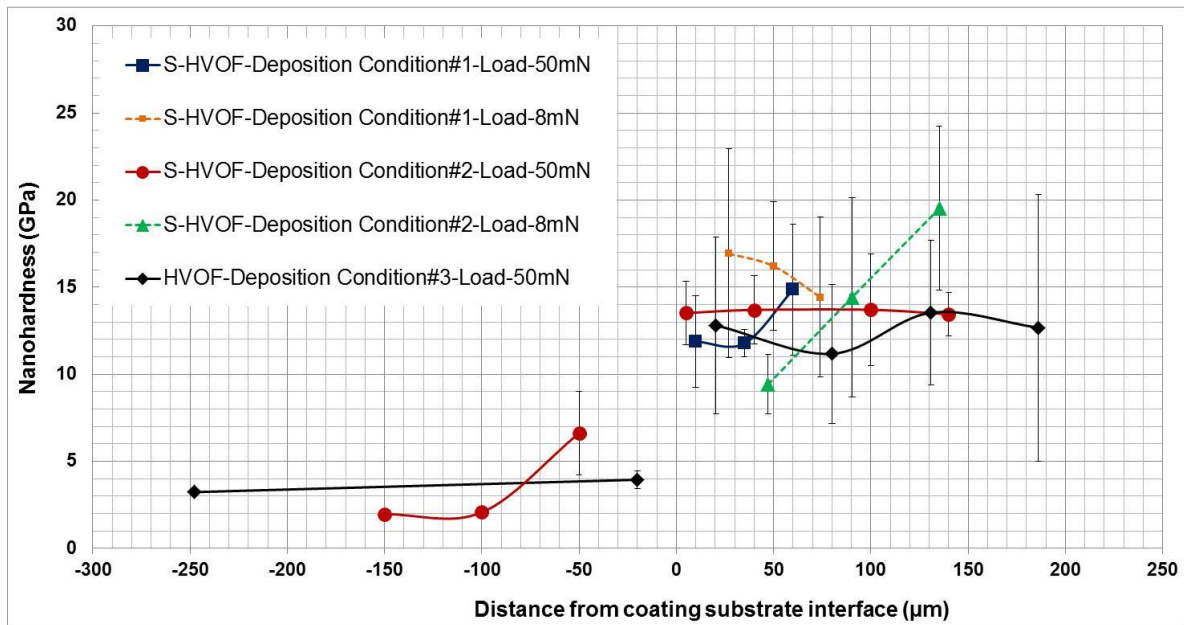


Figure 13, Nanoindentation results of coating substrate systems deposited under deposition conditions # 1, 2, 3. Zero at x-axis represents the location of coating-substrate interface and the distances represented are measured from this interface.

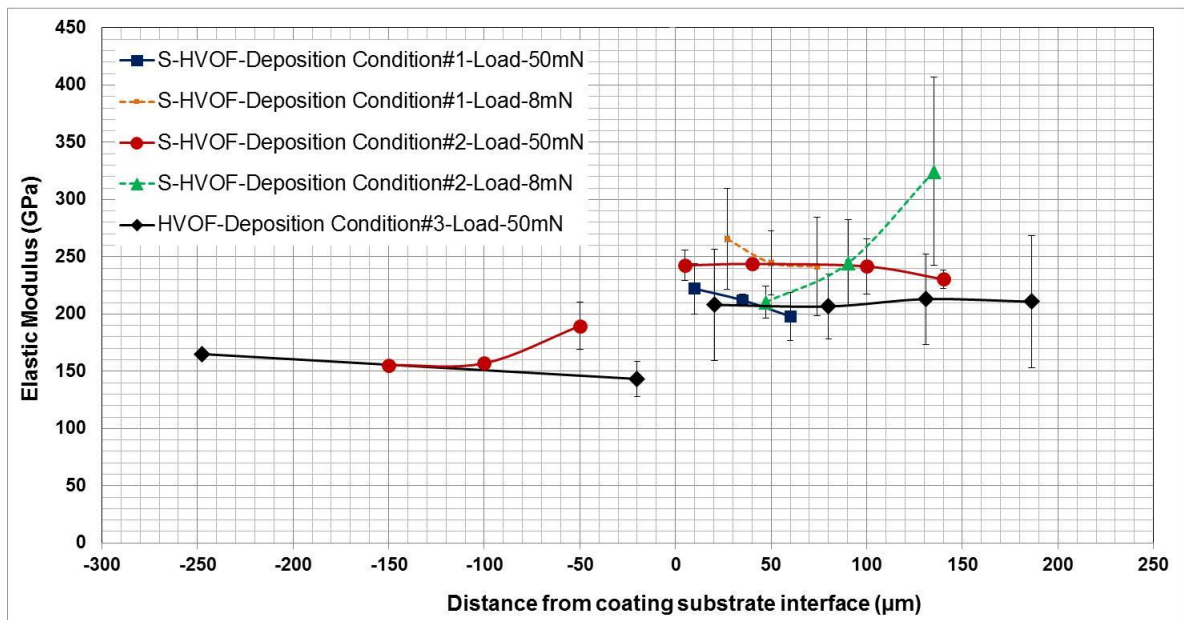


Figure 14, Reduced elastic modulus results of coating substrate systems deposited under deposition conditions # 1, 2, 3. Zero at x-axis represents the location of coating-substrate interface and the distances represented are measured from this interface.

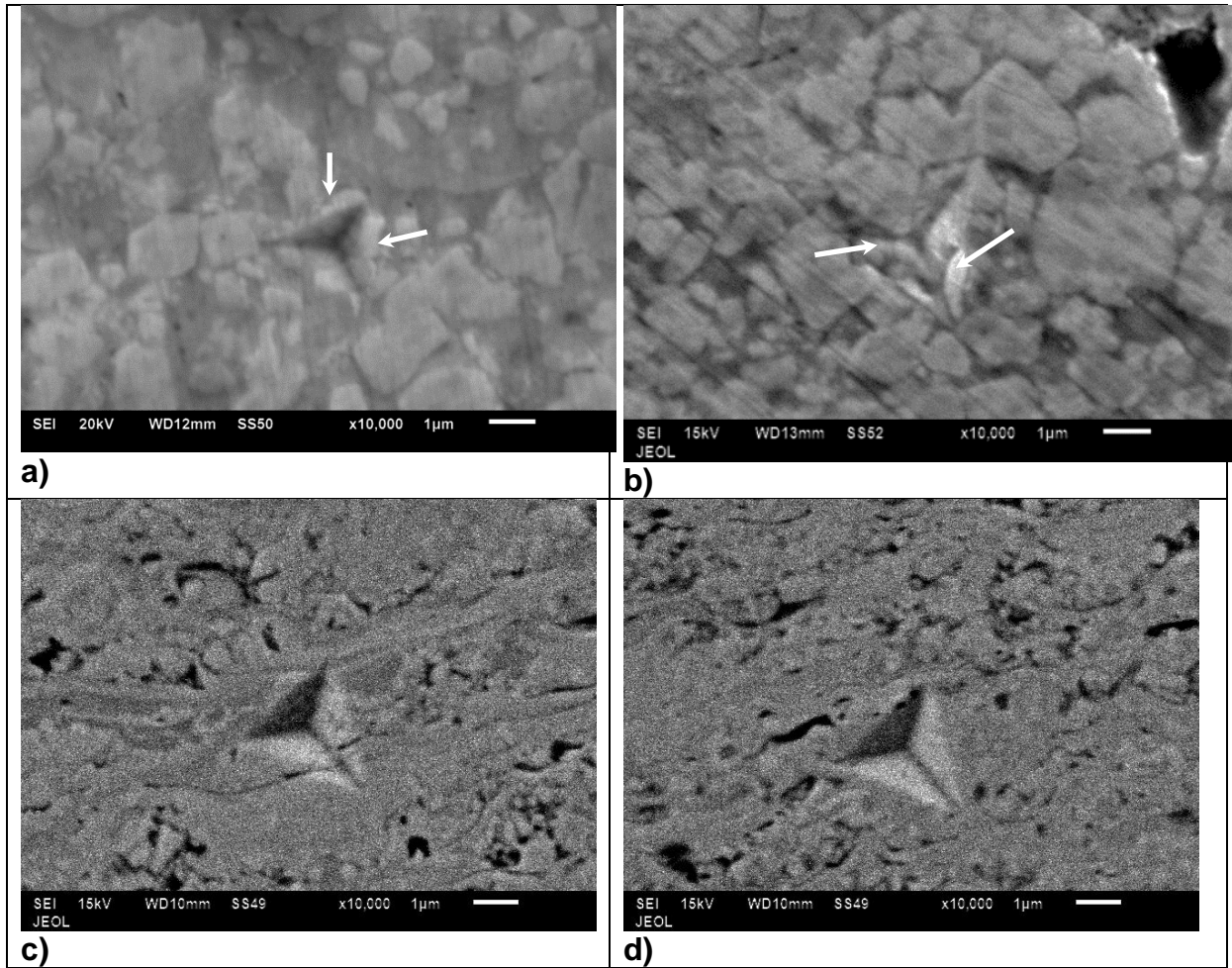


Figure 15, SEM observations of nanoindentations at 50mN load for a,b) conventional HVOF coatings (deposition condition # 3), c,d) S-HVOF coatings (deposition condition # 2). Arrows marked in caption a) indicate material pile-up, whereas in caption b) indicate carbide fracture.

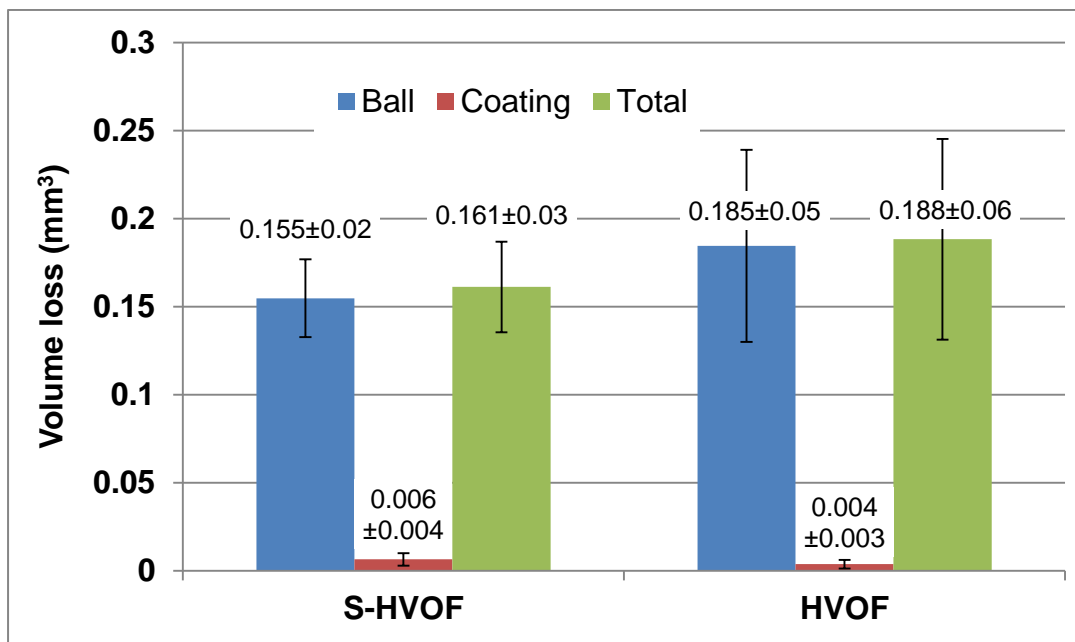
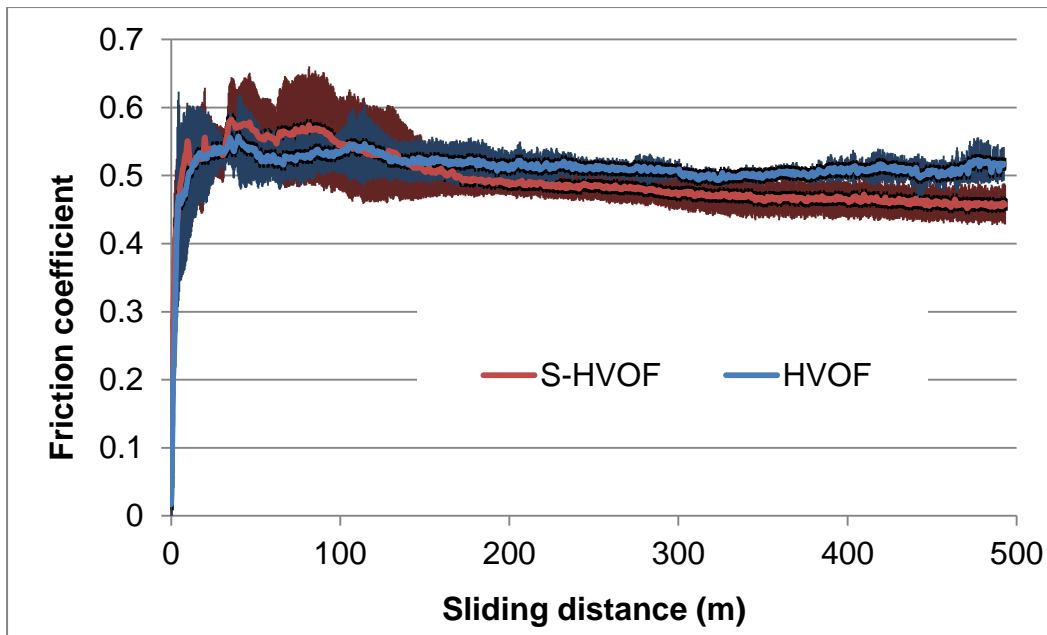
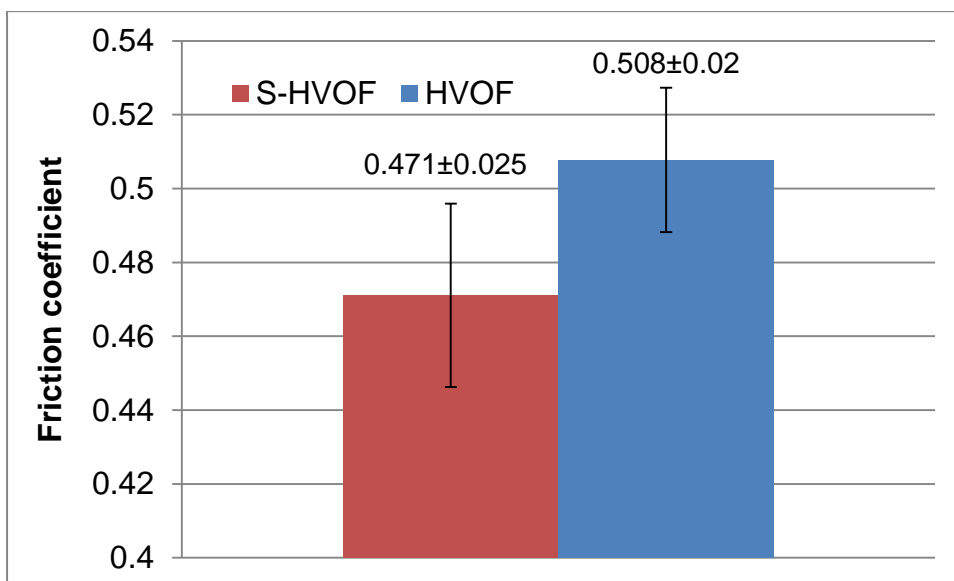


Figure 16, Volume loss results for the ball-on-plate sliding wear tests for S-HVOF (Deposition condition # 2) and HVOF (Deposition condition # 3) coatings.

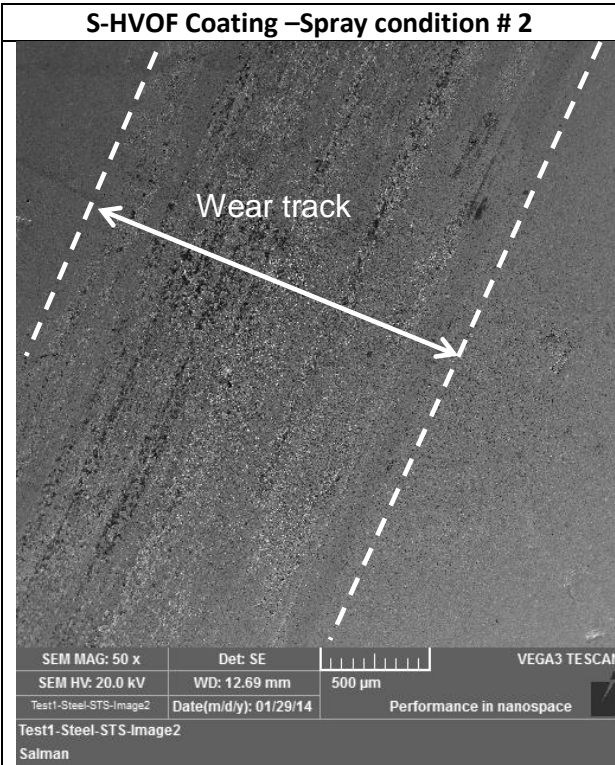


a)

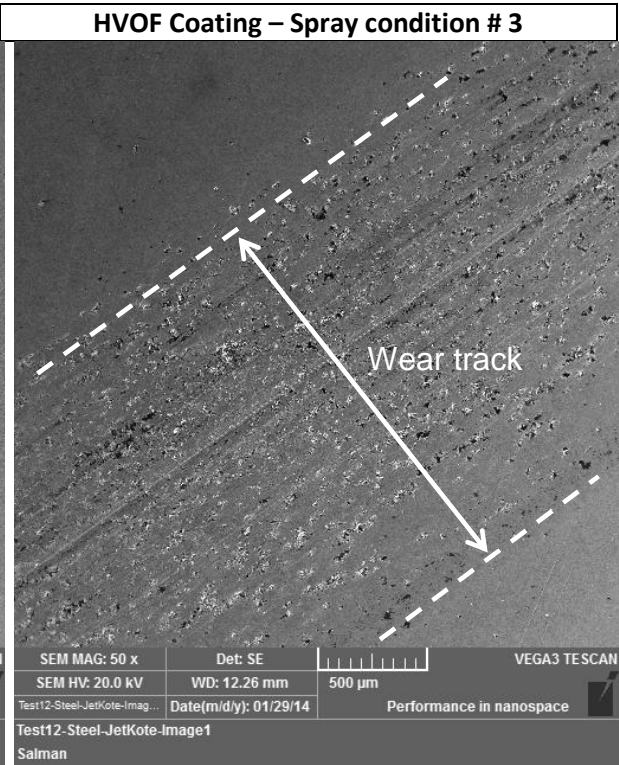


b)

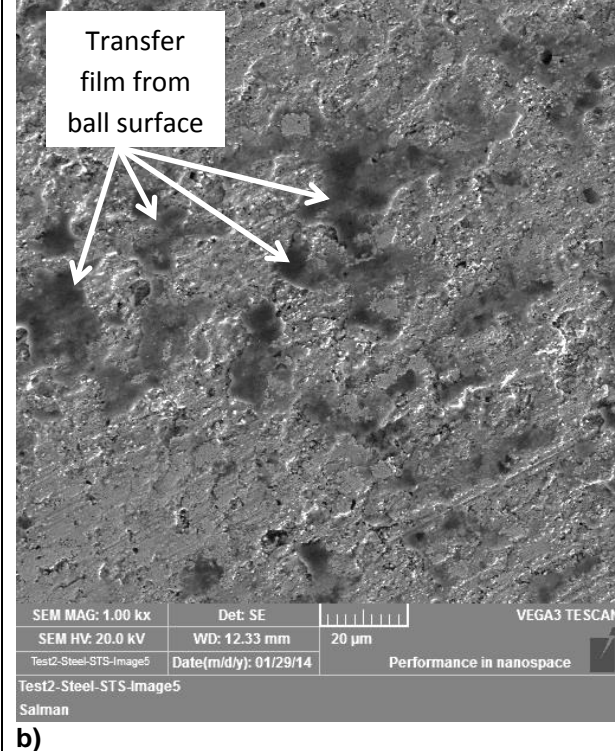
Figure 17, Average friction coefficient values for the ball-on-plate sliding wear tests for S-HVOF (Deposition condition # 2) and HVOF (Deposition condition # 3) coatings; a) average friction coefficient values with standard deviations, b) averaged steady-state friction values between 200m to 500m sliding distance.



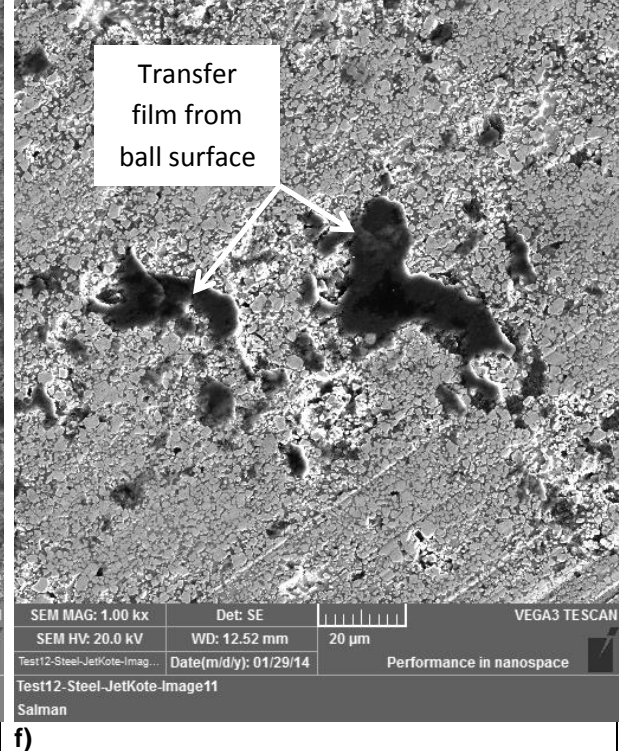
a)



e)



b)



f)

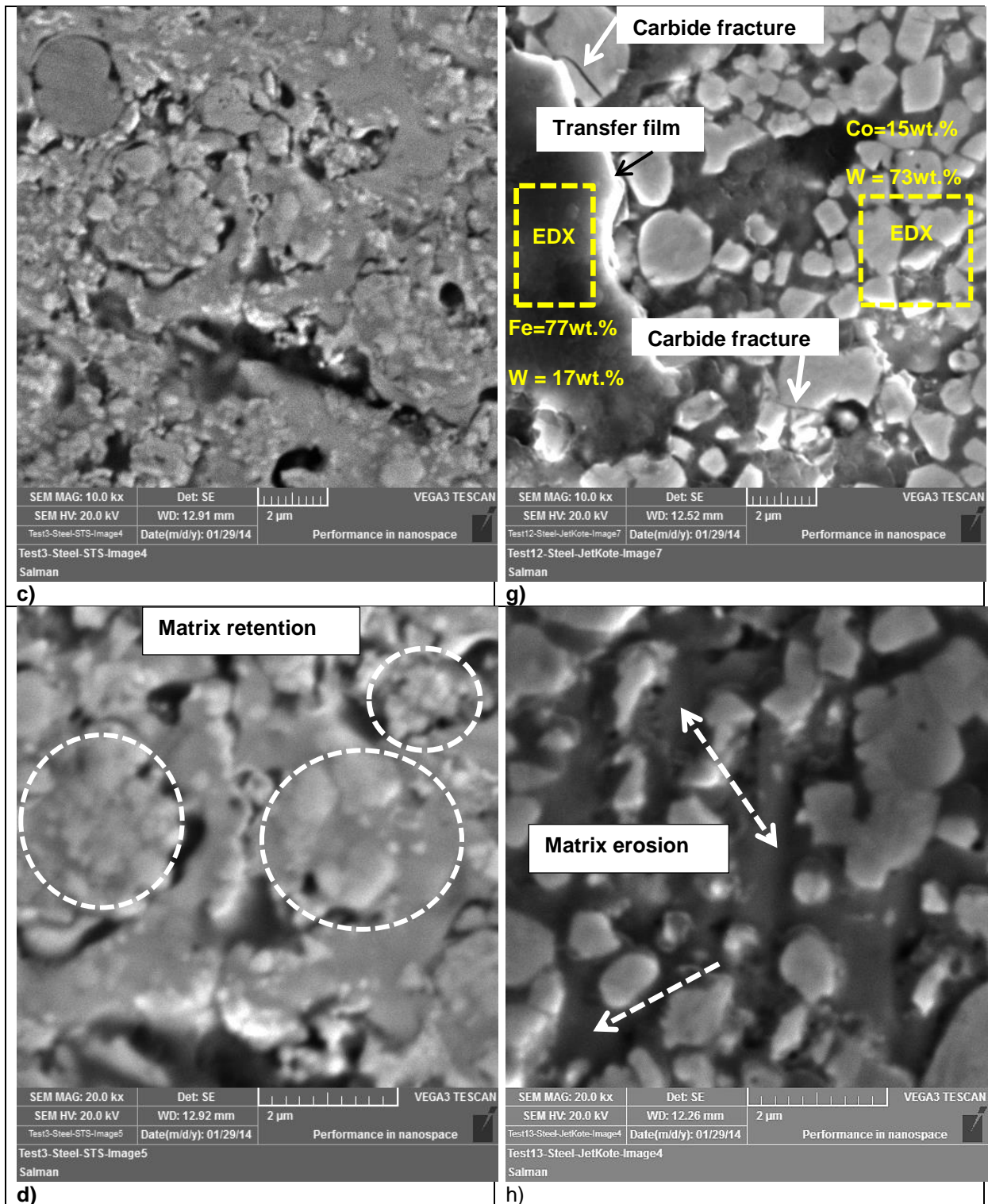


Figure 18, SEM Observations of the wear tracks of coatings deposited under spray conditions; a,b,c,d) # 2 and e,f,g,h) # 3. EDX analysis at two different location marked by boxes is shown in caption (g).

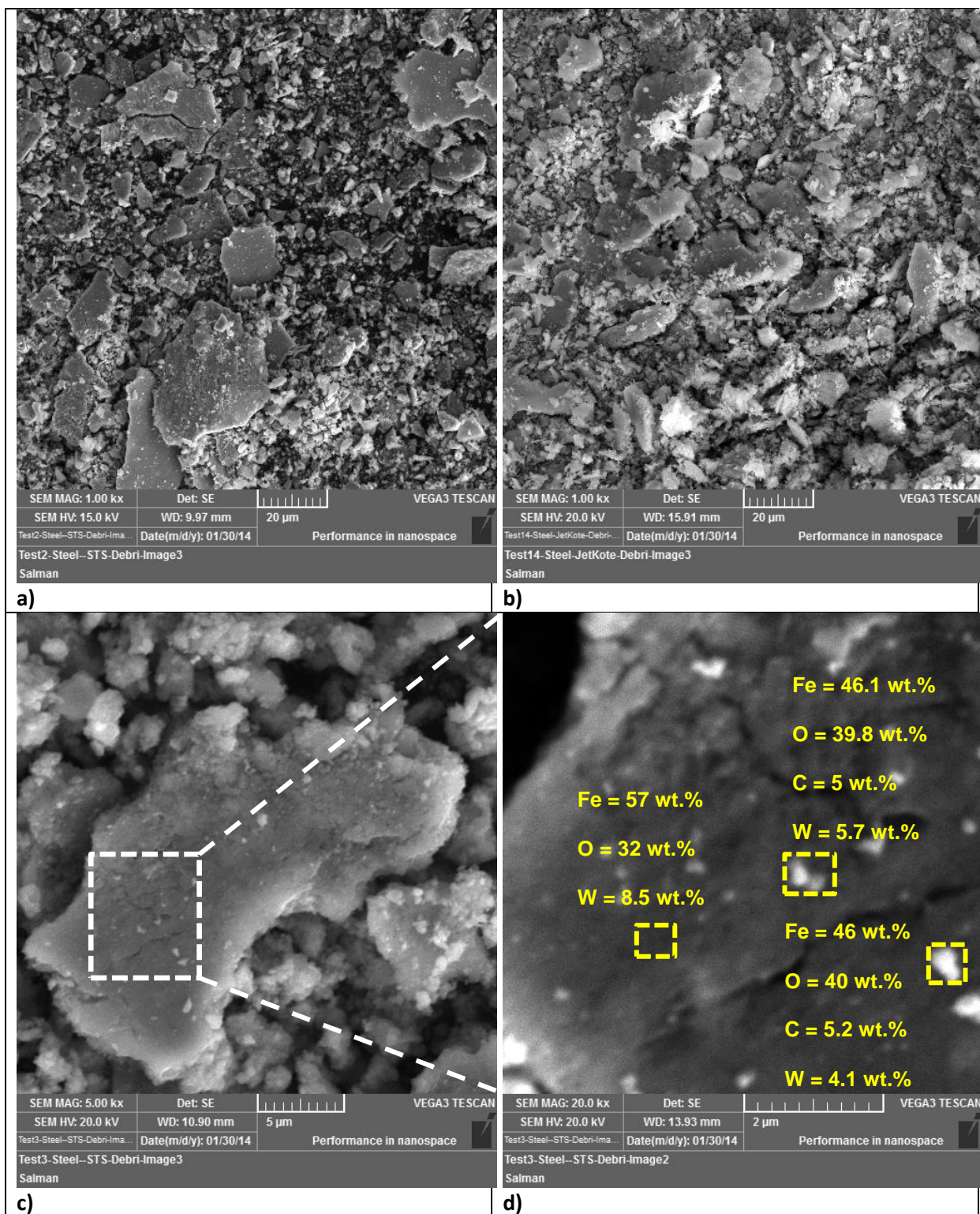


Figure 19, SEM Observations of the wear debris resulting from wear tests for test couples deposited under spray conditions a) #2 and b) #3, c) high magnification image of debris for spray condition # 2 indicating the location of EDX analysis, d) EDX analysis at three different locations marked with boxes.

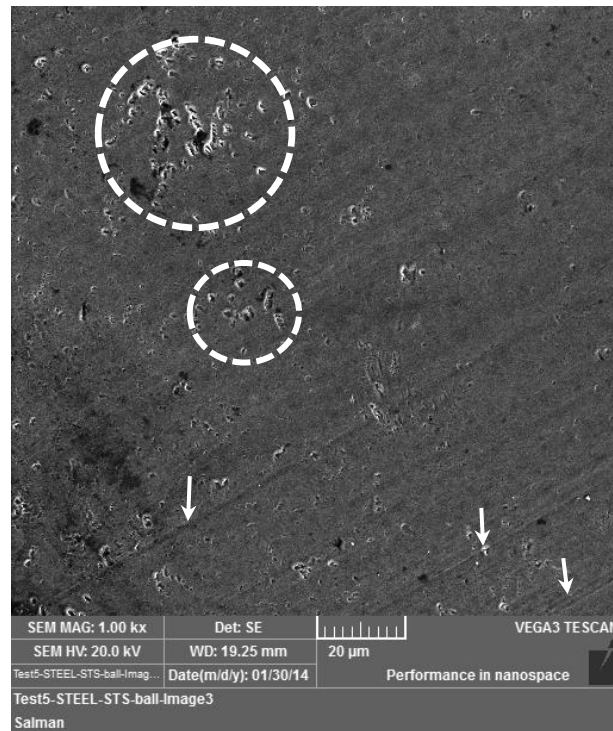


Figure 20, SEM Observations of the worn steel ball surface. The white arrows indicate the location of abrasive marks, whereas the dotted circle indicates the location of surface pits due to plastic deformation.